Effects of the convective field on weakly outgassing comets

A. Beth[★] and M. Galand[★]

Department of Physics, Imperial College London, Prince Consort Road, London SW7 2AZ, UK

ABSTRACT

By applying a kinetic approach, we have developed two models in order to assess the influence of one main driver of plasma acceleration, the convective electric field, on the cometary ion distribution at 67P/Churyumov-Gerasimenko (67P/C-G). This electric field is carried by the solar wind and corresponds to the acceleration undergone by cometary ions ultimately picked up. We have quantified its contribution on ion number density and mean velocity profiles, supported by an intercomparison with the recent literature. We found that the ion number density should reflect a departure from the observed $\sim 1/r$ law. We discuss reasons for this discrepancy.

Key words: plasmas – Sun: UV radiation – comets: individual: 67P.

1 INTRODUCTION

For two years, from 2014 August to 2016 September, the European Space Agency's *Rosetta* mission escorted comet 67P/Churyumov–Gerasimenko (Churyumov & Gerasimenko 1972, hereafter referred as 67P/C-G) between 3.8 au and perihelion at 1.24 au, reached in 2015 August. During that time, the cometary activity, expected to reach $Q = 4 \times 10^{27} - 8 \times 10^{27}$ molecules s^{-1} (Hanner et al. 1985; Benna & Mahaffy 2006; Hansen et al. 2007; Lamy et al. 2007; Tenishev, Combi & Davidsson 2008), was observed to be highly variable and with a heterogeneous coma (Hässig et al. 2015; Fougere et al. 2016), as probed *in situ* by the Rosetta Orbiter Spectrometer for Ion and Neutral Analysis (ROSINA)/Comet Pressure Sensor (COPS) and ROSINA/Double Focus Mass Spectrometer (DFMS) (Balsiger et al. 2007) and confirmed by other sensors (Hansen et al. 2016). During the escort phase, ROSINA/COPS observed an outgassing rate between 5×10^{25} and 4×10^{28} s^{-1}, namely an evolution over 3 orders of magnitude (Hansen et al. 2016). Observations from ROSINA/COPS also confirmed that the neutral number density has a $1/r^2$-dependence, relative to the cometocentric distance r (Bieler et al. 2015; Hässig et al. 2015).

For comparison, the ESA *Giotto* mission probed the coma of 1P/Halley over a few hours at a heliocentric distance of 0.89 au. The outgassing rate was estimated to be $Q = 6.9 \times 10^{29}$ s^{-1} ±50 per cent (Reinhard 1986), 1–2 orders of magnitude higher than at 67P/C-G near perihelion. At that heliocentric distance, *Giotto* observed well-defined boundaries and regions around 1P/Halley, such as:

(i) a diamagnetic cavity: close to the comet, there was a sharp drop in the magnetic field strength from 50 to 0 nT (Neubauer et al. 1986), consistent with the balance between the magnetic pressure and the ion-neutral drag (Cravens 1987; Ip & Axford 1987),

(ii) a contact surface: transition between a magnetic pile-up region and the diamagnetic cavity. The ion number density exhibited a sharp decrease and a different behaviour below and above the boundary. Below, the ion number density seemed to follow a $1/r$ dependency, whereas above, it followed $1/r^2$ (Balsiger et al. 1986; Altwegg et al. 1993)

These characteristic, cometary features result from the interaction between the solar wind and ions of cometary origin (Ip 2004). Magnetic field drops have been observed at 67P/C-G (Goetz et al. 2016a,b) by RPC/fluxgate MAGnetometer (Glassmeier et al. 2007) as well. Goetz et al. (2016a) determined an empirical law, depending on the cometary activity for the diamagnetic cavity radius. Nevertheless, recent literature has shown otherwise that the previous balance found at 1P/Halley for the contact surface does not hold and the cavity is more extended than originally predicted with a very dynamic boundary.

During the cometary escort phase, *Rosetta* probed the coma and its plasma properties with a wider range of conditions than at 1P/Halley, at different heliocentric distances and activity levels, from a few kilometres to a few hundred kilometres from the surface over the course of a day or over different seasons, giving us the opportunity to better understand the complex relation between the comet and the solar wind.

At a heliocentric distance of 3 au, ROSINA/DFMS observed the presence of refractory species, revealing that, during the low cometary activity phase, the solar wind was able to penetrate through the coma and cause the surface to sputter (Wurz et al. 2015). With the same sensor, it was possible to derive the ion composition which attested of a cometary origin (Fuselier et al. 2015), dominated by H_2O^+ and H_3O^+ water ions. From the *Rosetta* Plasma Consortium (RPC)/LAngmuir Probe (LAP) (Eriksson et al. 2007), Edberg et al. (2015) showed that for cometocentric distances between 10 and 250 km, the observed electron number density decreased overall as $\sim 1/r$. In addition, they derived an ion-to-neutral number density

★ E-mail: abeth@ic.ac.uk (AB); m.galand@imperial.ac.uk (MG)

ratio of $\sim 1 - 2.10^{-6}$. This is consistent with a coma outgassing radially at constant velocity, ionized by solar extreme ultraviolet radiation and energetic electrons (Galand et al. 2016) and with the ion velocity equal to the neutral one (Galand et al. 2016; Vigren et al. 2016). A constant ion velocity is however not a suitable assumption very close to the surface: in that case, adiabatic expansion needs to be taken into account, as observed on 2016 September 30 at the end of mission (Heritier et al. 2017a). The plasma seems to be composed of two electron populations: one dense and warm (Odelstad et al. 2015; Galand et al. 2016), the other, more rarefied and hot to super-hot (Broiles et al. 2016; Madanian et al. 2016). Near perihelion, a cold population is also present (Eriksson et al. 2017).

Finally, based on RPC/Ion and Electron Sensor (IES) (Burch et al. 2007) and RPC/Ion Composition Analyzer (ICA) (Nilsson et al. 2007), the solar wind particles were observed to be deflected by a few tens of degrees close to the nucleus and underwent mass loading (Broiles et al. 2015; Nilsson et al. 2015a,b; Behar et al. 2016). The newborn ions supply a new plasma component and gain energy from their interaction with the solar wind. Consequently, the solar wind has to be deflected to conserve the total plasma momentum (Glassmeier 2017). However, further away, the direction of H_2O^+ ions fits well the one of $E_{conv} = -v_{SW} \times B$, the convective or motional electric field (Behar et al. 2016). Simulations have been carried out to assess the effect of this electric field on the ion number density (e.g. Vigren et al. 2015; Madanian et al. 2016).

Near perihelion, the comet behaviour was different with a higher cometary activity (outgassing rates reached 5×10^{28} s^{-1}; Hansen et al. 2016), so that the ion-neutral chemistry could take place before the ions were lost through transport (Fuselier et al. 2016) and new ion species could be produced (Beth et al. 2016; Heritier et al. 2017b). This constrains the potential acceleration of newborn cometary ions: if there is a strong acceleration within the cavity (where *Rosetta* was at that time), it would prevent the chemistry from occurring. However, above the ion exobase, also referred as the collisionopause (Mandt et al. 2016), significant acceleration has been observed affecting the chemistry and the H_3O^+/H_2O^+ ratio (Fuselier et al. 2016). *Rosetta* was observed to be often within or close to the diamagnetic cavity (Goetz et al. 2016b, 2016a). Within such a region, there is no convective electric field as the magnetic field B drops to zero. Nevertheless, the ambipolar electric field is present, to ensure the quasi-neutrality. Indeed, the newborn photo-electrons have a very high bulk velocity compared with ions, and leave the comet faster (e.g. Cravens 1987). The ambipolar field would ensure the quasi-neutrality by accelerating ions and slowing down electrons, affecting the ion number density and the chemistry (Vigren & Eriksson 2017). Finally, the solar wind protons completely disappeared over the whole summer 2015 as *Rosetta* was getting close to and, at times, was within the cavity. The water ion energy dropped to values similar to the spacecraft potential (Mandt et al. 2016) and the hot electron energy distribution decreased significantly (Nemeth et al. 2016; Madanian et al. 2017) within the cavity.

In this paper, we have kinetically modelled the contribution of the effect of the solar wind convective electric field within the cometary ionosphere of 67P/C-G. The sections are organized as follows.

In Section 2, we present the theory and evaluate the effect of the convective electric field on the cometary ions from Model A (Section 2.1) and Model B (Section 2.2), and compare one to the other (Section 2.3),

In Section 3, we compare the results from Model B with existing works. In particular, we compare with the widely used Haser model

(Section 3.1) and with the recent work done by Madanian et al. (2016),

In Section 4, we conclude by summarizing what we have learned from this modelling work, highlight the potential limits and strengths of the models presented, and discuss future investigations to be undertaken in the context of Rosetta observations.

2 THEORY

In this section, employing a collisionless kinetic approach, we propose to model the effect of the convective electric field on ion number density and to assess the first three moments of the distribution function at large heliocentric distances. We have developed two models: Model A (Section 2.1), which has two dimensions in position and three in velocity (2D+3D) and Model B (Section 2.2, 2D+1D), built upon stronger assumptions. We present a comparison between these two models in Section 2.3.

2.1 Model A: 2D (position) × 3D (velocity) kinetic collision-free model

2.1.1 Theory and model

In this section, we provide the full description of Model A along with its assumptions.

2.1.1.1 Trajectories of ions. Model A describes the distribution function of newborn cometary ions in the vicinity of comet 67P/C-G at large heliocentric distances where outgassing rates are low enough, such that any ion-neutral chemistry and optical depth effect for EUV ionizing radiation can be neglected.

As these newborn cometary ions are immersed within the solar wind plasma, they are picked up by the solar wind convected magnetic field B. Assuming that the solar wind is a non-resistive plasma, the electric field in the frame of the solar wind should be 0 and the solar wind satisfies Ohm's law:

$$E_{conv} + \langle v_{SW} \rangle \times B \approx 0 \tag{1}$$

where $\langle v_{SW} \rangle$ is the solar wind mean speed and E_{conv}, the so-called convective electric field, required to ensure that the electric field vanishes in the solar wind rest frame. However, close to the surface, the cometary plasma number density overwhelms the solar wind density; one should consider to use the mean plasma velocity $\langle v_{plasma} \rangle$, between cometary ions and solar wind protons, instead of $\langle v_{SW} \rangle$ in equation (1) (e.g. Galand et al. 2016). For the rest of this paper, we have neglected such a feedback on the electric field and considered the effect of the solar wind alone. Thus, the trajectory of cometary ions is described by

$$m \frac{dv}{dt} = q(E_{conv} + v \times B) = q(v - \langle v_{SW} \rangle) \times B \tag{2}$$

where m is the mass of the ion, q, its charge and v, its velocity along its trajectory. As the initial ion velocity ($\sim 500 - 800$ m s^{-1}; see Section 3.3 of Galand et al. 2016 and references therein) is significantly lower than that of the solar wind ($\sim 400 - 800$ km s^{-1}), the ion trajectory is decomposed in two components:

(i) a constant drift at $\langle v_{SW} \rangle$,
(ii) a motion of gyration in the perpendicular direction with the gyroradius $r_g \sim m v_{\perp,SW}/qB$, where $v_{\perp,SW}$ is the perpendicular component of the solar wind velocity with respect to B.

However, as the interplanetary magnetic field is around 10^{-9} T and the solar wind velocity is between 400 and 800 km s^{-1}, the

gyroradius of newborn water ions (major component of cometary ions) is about 7.5×10^4 km. For our simulation, we explore the distribution function characteristics up to 20 km from the comet so that we can neglect this motion of gyration ($q\boldsymbol{v} \times \boldsymbol{B}$). Thus, close to the comet where the ion velocity is still $\ll \|\langle\boldsymbol{v}_{SW}\rangle\|$, ions experience a primarily constant acceleration $-q\langle\boldsymbol{v}_{SW}\rangle \times \boldsymbol{B} = q\boldsymbol{E}_{conv}$, since $\|\boldsymbol{E}_{conv}\| \gg \|\boldsymbol{v} \times \boldsymbol{B}\|$. These conditions hold as long as the simulation box size is $\ll r_g$.

Under these assumptions, the trajectory of ions is a parabola for which we propose an unusual parametrization in Section 2.1.1.2 (see also Appendix B).

2.1.1.2 Distribution function. For Model A, we assume for the newborn ions that:

(i) they are H_2O^+, produced only by photo-ionization of H_2O,

(ii) collisions with another species are neglected. The outgassing rate is sufficiently low to prevent any further reactions with other species, especially water molecules (to destroy H_2O^+ and to produce H_3O^+) and spectral absorption by water,

(iii) at the time of their production, they have a distribution function of the same form as that of the neutrals, i.e. a Maxwellian distribution $f_n(\boldsymbol{v})$ centred at $U_n = 650$ m s^{-1} in the radial direction, 0 in the transverse ones, with a velocity dispersion $\sigma_n = 0.3U_n$ (corresponding to $T \sim 83$ K) in all directions,

(iv) steady-state is assumed.

Under these assumptions, the distribution function of ions is the solution of the reduced Boltzmann equation:

$$\frac{\partial f(\boldsymbol{r}, \boldsymbol{v})}{\partial t} + \nabla_{\boldsymbol{r}} \cdot (\boldsymbol{v}f) + \nabla_{\boldsymbol{v}} \cdot (\boldsymbol{a}f) = v_s\frac{\mathrm{d}f(\boldsymbol{r}, \boldsymbol{v})}{\mathrm{d}s} = P_{ion}(\boldsymbol{r}, \boldsymbol{v}) \quad (3)$$

where $\boldsymbol{a}$ is the acceleration induced by external and fictitious forces, $\nabla_{\boldsymbol{r}}\cdot$ is the divergence with respect to the position coordinates, $\nabla_{\boldsymbol{v}}\cdot$, with respect to the velocity coordinates, s is the distance along the trajectory of an ion in the 6D phase space, v_s, the absolute velocity of the ion, f, the distribution function of ions in the velocity space, and P_{ion}, the ion production rate from photo-ionization. Because collisions are neglected and the forces are conservative, the system is deterministic: the trajectory in the position and velocity coordinates is perfectly known and is a function of initial conditions and of time.

The ion production rate, P_{ion} due to photo-ionization, is given by:

$$P_{ion}(\boldsymbol{r}, \boldsymbol{v}) = \nu_{ion}n_n(r)f_n(\boldsymbol{v}) = \frac{\nu_{ion}n_n(r)}{(2\pi\sigma_n^2)^{\frac{3}{2}}}\exp\left(-\frac{(\boldsymbol{v} - U_n\boldsymbol{e}_r)^2}{2\sigma_n^2}\right) \quad (4)$$

where the photo-ionization frequency $\nu_{ion} = 6.10^{-8}$ s^{-1} (see Table 1), independent of r (as the coma is assumed optically thin), and $n_n(r)$, the neutral number density from the comet. We warn the reader here that this production rate has the inconvenience to be invariant by rotation in positon but not by translation, important for the symmetry of the problem. The neutral density is derived by assuming a constant outgassing rate Q at the surface and a constant outflow velocity U_n with a spherical symmetry and ignore any chemical loss or production of neutrals in the coma which is justified at the cometocentric distances considered (Haser 1957):

$$n_n(r) = \frac{Q}{4\pi U_n r^2} \quad (5)$$

Because we combine the spherical symmetry of the comet and the constant direction of $\boldsymbol{E}_{conv}$, the most appropriate coordinate system is the cylindrical one with the direction z along $-\boldsymbol{E}_{conv}$, so that our modelling is invariant by rotation around z.

Table 1. For Model A (Section 2.1) and Model B (Section 2.2): key parameters used as inputs to drive each model in order to compare one with the other (2) (Section 2) with Haser (1957) (H) (Section 3.1) and Madanian et al. (2016) (M) (Section 3.2)

Physical inputs	Notation (unit)	Value	A	B
Outgassing rate	Q (s^{-1})	$10^{26(M)}$		×
		$10^{27(2, H)}$	×	×
Neutral radial velocity	U_n (m s^{-1})	$650^{(2, H)}$	×	×
		$1000^{(M)}$		×
Photo-ionization rate	ν_{ion} (s^{-1})	$6.10^{-8(2, H)}$	×	×
		$1.10^{-7(M)}$		×
Comet's radius	r_c (m)	$2.10^{3(2, M, H)}$	×	×
Convective electric field	E_{conv} (V m^{-1})	$5.10^{-4(2, M)}$	×	×
Neutral dispersion velocity (only relevant for Model A)	σ_n (m s^{-1})	195	×	

In this frame, the distribution function of ions is derived from equation (3) and Appendix A as follows:

$$f(\boldsymbol{r}, \boldsymbol{v}) = \int_{-\infty}^{S} P_{ion}(\boldsymbol{r}_0(s), \boldsymbol{v}_0(s))\frac{\rho_0(s)}{\rho}\frac{\mathrm{d}s}{v_{s_0}}$$

$$= \int_{-\infty}^{T} P_{ion}(\boldsymbol{r}_0(t), \boldsymbol{v}_0(t))\frac{\rho_0(t)}{\rho}\mathrm{d}t \quad (6)$$

where

(i) $\boldsymbol{r}$ is the position where we 'calculate' the ion-associated distribution function and ρ, the associated distance from the z-axis,

(ii) $\boldsymbol{v}$ is the velocity at which we 'observe' the ion,

(iii) $\boldsymbol{r}_0$ and $\boldsymbol{v}_0$ are the position and the velocity of the ion along the trajectory, respectively, $v_{s_0} = \|\boldsymbol{v}_0\|$, ρ_0 is the distance of the ion from the z-axis during its motion,

(iv) s is the coordinate along the trajectory, $\boldsymbol{r}_0(S) = \boldsymbol{r}$ and $\boldsymbol{v}_0(S) = \boldsymbol{v}$

In Appendix A, we provide details about why we introduce the factor ρ_0/ρ, consequence of the system of coordinates we have used.

This is not simple to derive a lower bound for the integration in time in equation (6) to prevent irrelevant calculations and computation time and/or find an optimized time step. To overcome these inconveniences, we propose a new parametrization for the trajectory of ions, detailed in Appendix B, not as a function of time but of the eccentric anomaly Ω of the parabola described by the ion, such as:

$$f(\boldsymbol{r}, \boldsymbol{v}) = \frac{m v_\perp}{q E_{conv}}\int_{-\pi}^{\omega}\frac{P_{ion}(\boldsymbol{r}_0(\Omega), \boldsymbol{v}_0(\Omega))}{1 + \cos\Omega}\frac{\rho_0(\Omega)}{\rho}\mathrm{d}\Omega \quad (7)$$

The numerical integration of the distribution function and its moments are described in Appendix C. For a numerical good estimation of the moments and the distribution function at each $\boldsymbol{r}_0$:

(a) we start with an initial velocity space grid. For each grid point, we integrate equation (7) to construct $f(\boldsymbol{r}, \boldsymbol{v})$,

(b) we calculate the moments of $f(\boldsymbol{r}, \boldsymbol{v})$,

(c) we use those moments to know where the distribution function has to be more precisely investigated (near the bulk),

(d) we update our grid and reintegrate equation (7) to evaluate $f(\boldsymbol{r}, \boldsymbol{v})$ on the new grid

(e) we start again at the step (b) and continue until the moments (here the zeroth-order one only) converge.

For each point of the velocity grid, we perform an integration along the trajectory of the ion. Altogether, we have a combination

of four integrals for the distribution function: one along the parabola in the position space and three in the velocity space.

Other crossed moments should be considered to estimate accurately our velocity distribution up to the second order. To this end, we determine also the covariance of the velocity:

$$n\sigma_{xy}(\boldsymbol{r}) = \int (v_x - \langle v_x\rangle)(v_y - \langle v_y\rangle)f(\boldsymbol{r}, \boldsymbol{v})\mathrm{d}^3\boldsymbol{v} = 0 \text{ by symmetry}$$

$$n\sigma_{xz}(\boldsymbol{r}) = \int (v_x - \langle v_x\rangle)(v_z - \langle v_z\rangle)f(\boldsymbol{r}, \boldsymbol{v})\mathrm{d}^3\boldsymbol{v}$$

$$n\sigma_{yz}(\boldsymbol{r}) = \int (v_y - \langle v_y\rangle)(v_z - \langle v_z\rangle)f(\boldsymbol{r}, \boldsymbol{v})\mathrm{d}^3\boldsymbol{v} = 0 \text{ by symmetry}$$

$$(8)$$

In Appendix D, we detail the derivation of minimum and maximum dispersions, as well as the angular deviation linked to the second-order centred moments.

2.1.2 Results from Model A

In this section, we present the results from the simulations for Model A (described in Section 2.1.1.1): the ion number density (2.1.2.2), the mean velocities (2.1.2.3), and the second-order centred moments (2.1.2).

2.1.2.1 Zeroth-order moment: ion number density. Fig. 1 (top, left-hand panel) shows the ion number density profile for a downward convective electric field. Based on equation (4), the production term and thus the distribution function are directly proportional to $\nu_{\text{ion}}Q = 6.10^{19}$ s^{-2} (see Table 1), so that the ion number density can be scaled accordingly as long as other parameters are not changed.

The ion number density, from 10^7 m^{-3} at 20 km to 10^9 m^{-3} at the cometary surface, is extremely variable close to the surface: high on the upward side ($z > 0$), low on the downward side ($z < 0$). On the upward side, the ions produced along the z-axis are repelled by the electric convective field towards the comet, so that the number density is not zero at the surface. However, on the downward side, the newborn ions are taken away from the surface, with the same force, leaving the ion number density at the surface to be zero.

In addition, the simulation produces a cometary wake (detailed in Appendix E), physical and numerical, within which the ion number density does not really seem continuous. Indeed, as mentioned in Section 2.1.1, the comet cuts the trajectory of some ions leading to discontinuities in the distribution function. To support this idea, we have determined the region which ions born at the surface can reach (see Appendix E). This limit is represented by a black line in Fig. 1. The discontinuities are linked to this boundary. As we estimate a function g, here the density and higher order moments, by a numerical integration, there are still numerical errors, proportional to the n-th derivative of the estimated function g: if the n-th derivative $g^{(n)}$ is discontinuous, the numerical error is not bounded any more.

Regarding the asymmetry between the $\pm z$ regions, the ion number density is higher for $z < 0$ than for $z > 0$ (for the same distance to the z-axis). On the one hand, for $z > 0$, ions present in this region have been all produced in it. On the other hand, for $z < 0$, ions can either have been produced in this region or come from the $z > 0$ region, where they were born.

Finally, the convective electric induces a strong asymmetry within the ion coma only in the first 10 km from the nucleus.

2.1.2.2 First-order moment: mean velocity. Fig. 1 (top, middle panel) shows the mean perpendicular velocity in the ρ-direction of ions between 0 and 650 m s^{-1} (the other component is perpen-

dicular to the figure and thus zero by symmetry). As the electric field is a conservative force applied to the z-direction, it does not affect the perpendicular velocity of the ions which is conserved during their motion of the ions. Consequently, the mean perpendicular velocity $\langle v_\perp\rangle$ has to be between 0 and $U_n \pm \sigma_n$ in absolute value, as observed.

$\langle v_\perp\rangle$ gives an insight into the initial location of ion production: $\langle v_\perp\rangle \approx 0$ means that the ions are mainly produced close to the z-axis whereas $\langle v_\perp\rangle \approx U_n$ means that the ions are mainly produced close to the $z = 0$ plane passing through the comet.

Fig. 1 (top, right-hand panel) shows the parallel mean velocity. This reveals extremely high velocities, between 0 and 6×10^3 m s^{-1}, even in the vicinity of the comet. Close to the surface on the upper side, the mean parallel velocity is nearly zero, whereas the newborn ions should have gone upward ($v_\parallel > 0$). This highlights that these same ions are coming back ($v_\parallel < 0$), repelled by the convective electric field such that the mean parallel velocity is low in magnitude.

Moreover, $\langle v_\parallel\rangle$ is increasingly downward, up to $\sim$6000 m s^{-1} ($\sim$6.5 eV) for decreasing z, showing that ions are strongly accelerated compared with their initial velocity, even at 20 km from the comet.

2.1.2.3 Second-order moments: mean dispersion and covariance. By providing the full ion distribution function, Model A allows us to derive any moments. It may be particularly interesting to go up to the second order as it is linked to the temperature/pressure of the ions.

Lower panels in Fig. 1 show the minimum and maximum dispersions, σ_{min} and σ_{max}, as well as the deviation Θ. This is reasonable to assume that there are two dispersions for the plasma, one in the parallel direction to the electric field and the other, perpendicular to it. Model A allows us to check this assumption.

The left, lower panel in Fig. 1 shows the minimum dispersion of the distribution function. This value is relatively close to the neutral dispersion, σ_n. Because we are dealing with a unidirectional, conservative force, there is one direction for which the dispersion should be unchanged. In the wake (Section 2.1.2.1 and Appendix E), the distribution is found to be cooler than in other regions but these are likely numerical features.

The middle, lower panel in Fig. 1 shows the maximum dispersion of the distribution function. This dispersion is high between 0 and 2.5×10^3 m s^{-1}, and of the same order of magnitude as the mean velocity $\langle v_\parallel\rangle$. Additionally, this dispersion and thus the temperature reflect a gradient (outwardly increasing) such that a constant temperature for ions cannot be assumed. Finally, the dispersion is higher for $z > 0$ than for $z < 0$. For $z > 0$, a few ions are coming from below, having been produced close to (ρ, z) depending on the strength of E_{conv}; there is also the contribution of ions with $v_z > 0$ and $v_z \sim \langle v_z\rangle$. All this explains the strong dispersion.

The right, lower panel in Fig. 1 shows the deviation of the maximum dispersion from the electric field direction, i.e. the orientation of our 3D distribution function, here around $\sim\pm5°$. For fluid and plasma modelling, one often assumes that there are two temperatures to describe the particles: parallel/perpendicular to the magnetic field. Here we make the analogy with the electric field. We would like to check how reasonable it is to consider such assumptions. By determining the covariance matrix (Appendix D), we can check how important non-diagonal terms are. They have to be small enough with respect to the diagonal terms to be able to reduce to parallel and perpendicular temperatures. The maximum angular deviation from the electric field direction is $\pm5°$, which means that two temperatures can be assumed, one along the electric field and the other
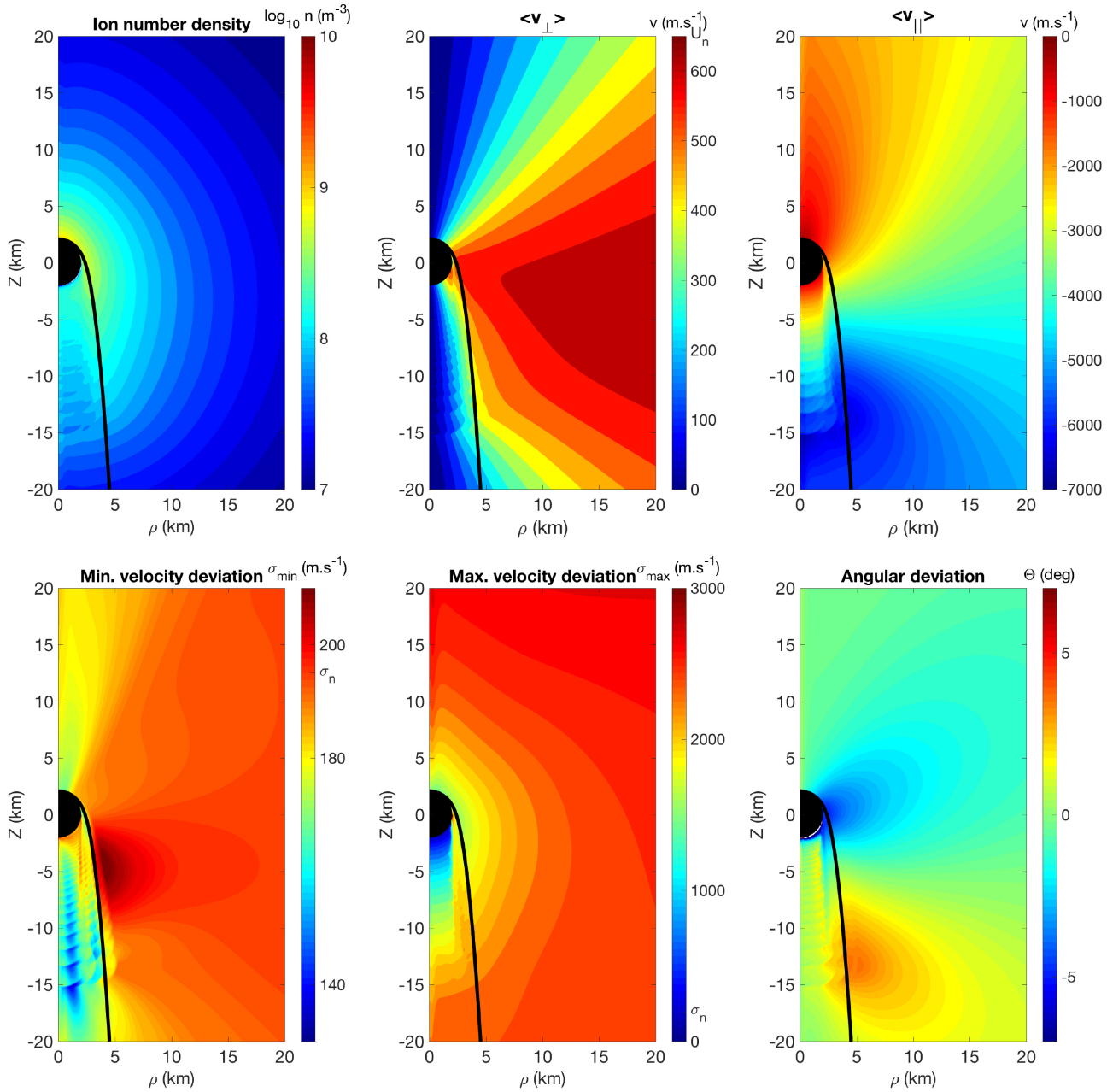
Figure 1. Zeroth, first, and second moments of the ion distribution function up to a cometocentric distance of 20 km from the comet for Model A. By cylindrical symmetry, the moments are plotted as a function of $\rho = \sqrt{x^2 + y^2}$ and z. Left, upper panel: ion number density (m^{-3}) in logscale for a downward convective electric field. Middle, upper panel: mean perpendicular velocity $(m\,s^{-1})$. By symmetry, the mean velocity in the perpendicular direction of the page is 0. Right upper panel: mean parallel ion velocity $(m\,s^{-1})$. Negative values mean that the ion flux is going in the same direction as the convective electric field. Left lower panel: minimal standard deviation σ_{min} $(m\,s^{-1})$ in linear scale for a downward convective electric field. Middle lower panel: maximal standard deviation σ_{max} $(m\,s^{-1})$. Right, lower panel: mean angular deviation Θ $(°)$. The black disc represents the comet with a 2-km radius. The black line demarcates the numerical wake (see Appendix E): the region which can only be reached by ions born at the surface. The inputs are listed in Table 1 (Model A, Section 2.1)

one, perpendicular to it. Equivalently, the pick-up ion process leaves the velocity parallel to the magnetic field unchanged and requires a full gyromotion to deflect the ion acceleration from the direction of $\boldsymbol{E}_{conv}$.

2.2 Model B: simplified 2D (position) × 1D (velocity) collision-free model

In this section, we present a second model, Model B, for describing the effect of the solar wind convective electric field on cometary

ions. It builds upon additional assumptions (e.g. no velocity dispersion for neutral) compared with Model A (see Section 2.1.1), but is less computationally expensive and can therefore be applied over a larger space domain.

2.2.1 Theory

The basis of this model is the previous work from Vigren et al. (2015) describing the effect of the solar wind convective electric field.
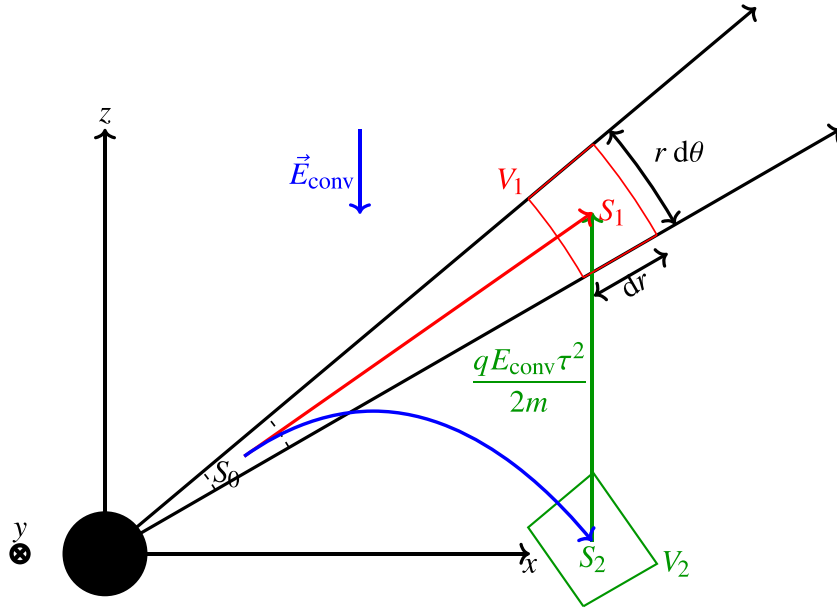
Figure 2. Representation of Model B. The ion, produced initially at S_0, reaches to the position S_1 in the absence of external forces but goes to S_2 in the presence of the convective electric field. The volume element from S_0 to S_1 expands as r_1^2/r_0^2. As we are considering a constant force – independent of the position – the volume element V_2 is equal to V_1. However, the volume V_2 is not a translation along z of the volume V_1 but a composition of stretching and rotation.

The ion is produced exactly radially (without any dispersion), at a given speed U_n corresponding to the bulk velocity of neutrals. In presence of only the solar wind $\boldsymbol{E}_{\text{conv}}$, the trajectory of the ion is given by:

$$\rho(t) = \rho_0 + v_{\rho_0} t$$

$$z(t) = z_0 + v_{z_0} t - \frac{q E_{\text{conv}}}{2m} t^2$$

$$v_\rho(t) = v_{\rho_0}$$

$$v_z(t) = v_{z_0} - \frac{q E_{\text{conv}}}{m} t \qquad (9)$$

from an original location (ρ_0, z_0) where the ion was produced radially with the initial velocity U_n separated in two components:

$$v_{\rho_0} = U_n \frac{\rho_0}{\sqrt{\rho_0^2 + z_0^2}}$$

$$v_{z_0} = U_n \frac{z_0}{\sqrt{\rho_0^2 + z_0^2}}$$

The 'philosophy' is to compare where the ion (produced at S_0) should have been without the convective electric field (position S_1) and where it is in its presence (position S_2) (Fig. 2). Let's use the subscript 1 for the position of the ion without external forces (radial motion of the ion) and 2 for the position in the presence of the convective electric field. The relation between both coordinates is given by

$$\rho_1 = \rho_2$$

$$z_1 = z_2 + \frac{q E_{\text{conv}}}{2m} t^2$$

$$v_{\rho_1} = v_{\rho_2}$$

$$v_{z_1} = v_{z_2} - \frac{q E_{\text{conv}}}{m} t \qquad (10)$$

The meaning is that the newborn ion, instead of reaching the position S_1, reaches position S_2. However, there is another point

which we have to worry about: does the initial volume element (in 3D) at S_0 stretch identically from S_0 to S_1 and from S_0 to S_2? The answer is yes and its rigorous demonstration is provided in Appendix F.

The ion number density is then given by (see Appendix F):

$$n_{\text{ion}}(x, y, z) = \int_I \nu_{\text{ion}} n_n \left(x, y, z + \frac{q E_{\text{conv}} \tau^2}{2m} \right) d\tau \qquad (11)$$

as derived by Vigren et al. (2015), except we have removed C_τ. We prefer to focus on $I \subset \mathbb{R}^+$, the interval of integration, instead.

Depending on the final position (x, y, z) of the ion, the interval I is different. There are three cases:

(i) outside the wake – where the wake is defined in Appendix E – the radial distance r_0 from the comet at which the ion is produced is higher than the cometary radius r_c. This means that $\forall \tau > 0$, the ion never crosses the comet $(r_0 > r_c)$ and then $I = \mathbb{R}^+$. For such a case, we have derived an analytical expression for the ion number density (see Appendix G),

(ii) inside the wake, but for $\rho = \sqrt{x^2 + y^2} < r_c$ and $z < 0$ (see Fig. 3, between the z-axis and the grey line). While for small τ, the ion is produced above the surface, there exists τ, τ_{max}, beyond which the ion is produced within the comet or has a trajectory crossing it before reaching S_2. For $\tau > \tau_{\text{max}}$ the integrand should be set to zero. Thus, $I = [0; \tau_{\text{max}}]$. Vigren et al. (2015) did not remove these ions from their simulation (i.e. they have performed the integration over $[\tau_2; +\infty[$ in addition). This leads to an overestimation by 40–60 per cent of the ion number density in this particular region for $E_{\text{conv}} = 1$ V m^{-1} (Vigren, private communication, 2017).[1] This is highlighted by the grey discontinuity on Fig. 3, where our ion number density and absolute mean parallel velocity are lower than theirs,

---

[1] However, for such a strong convective electric field, considering the usual solar wind speed, the gyroradius is about 30 km, of the order of the simulation box size used here.
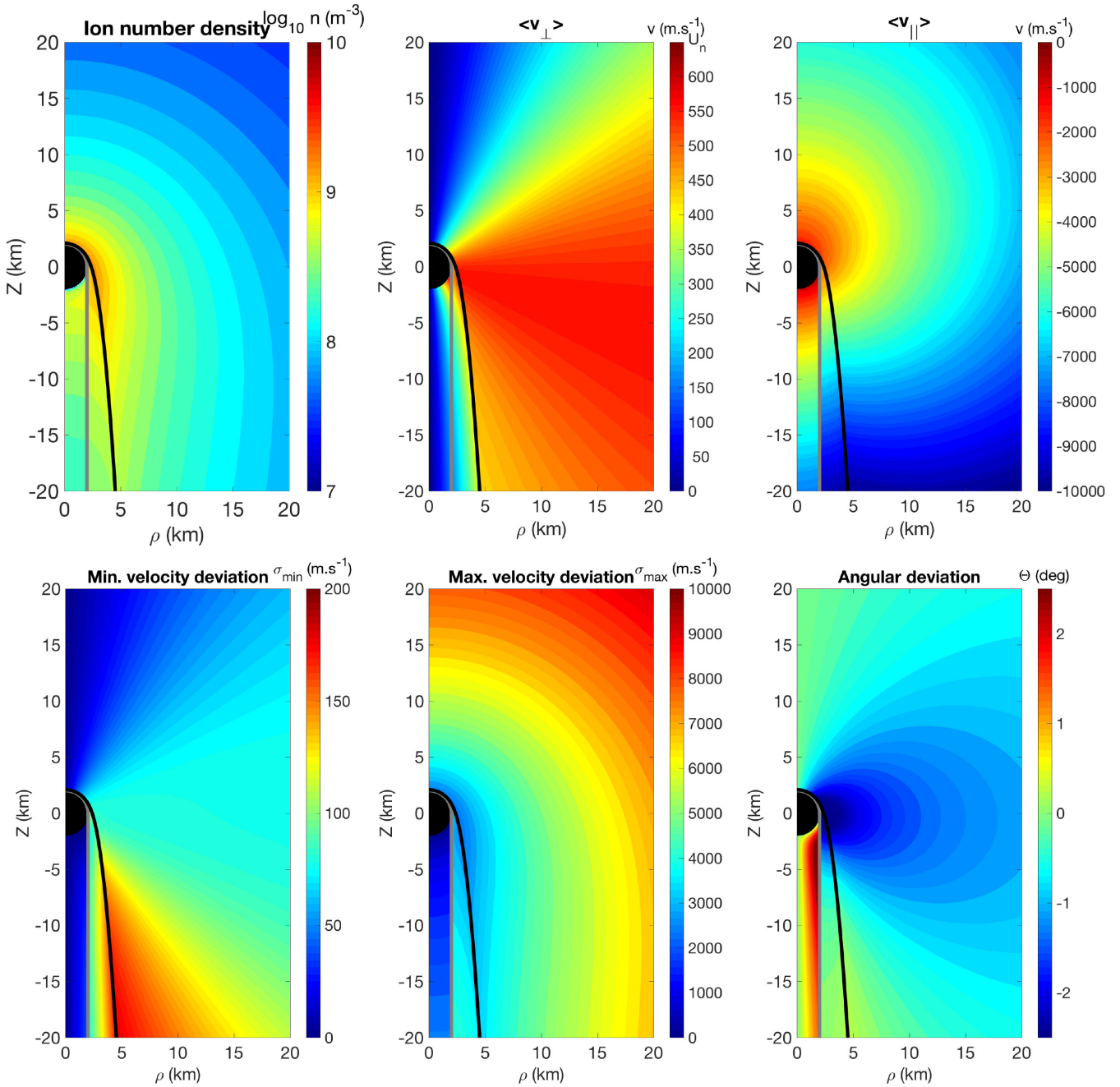
Figure 3. Same as in Fig. 1, but for Model B, with the same inputs as used for Model A in Section 2.1 (see Table 1). The range of values for the colour bars is however different from Fig. 1. In addition, an additional boundary has been plotted in grey, following the surface for $z > 0$ and such that $\rho = r_c$ for $z < 0$.

(iii) inside the wake, but for $\rho = \sqrt{x^2 + y^2} > r_c$ or $z > 0$ (see Fig. 3, between the grey and black lines), the initial production site of the ion gets closer and closer to the comet with increasing τ, crosses the surface of the comet, and crosses or not the z axis. It ultimately reaches the part of the position space for $z > 0$ and $0 < \theta < \pi/2$. This means that I is defined by two characteristic times, τ_1 and τ_2. For increasing τ from $\tau = 0$, the first corresponds to the time at which the production site moves from outside to inside of the comet. The second corresponds to the opposite. Thus, $I = \mathbb{R}^+ \setminus [\tau_1; \tau_2] = [0; \tau_1] \cup [\tau_2; +\infty[$. The previous case (for which $\rho < r_c$ and $z < 0$) is equivalent by setting $\tau_1 = \tau_{\text{max}}$. and $\tau_2 = +\infty$.

For some of these cases, we have to determine the initial location (ρ_0, z_0) of the ion where it is produced as a function of ρ, z, and τ. Its initial position is given by:

$$r_1(\rho, z, \tau) = \sqrt{\rho^2 + \left(z + \frac{q\,E_{\text{conv}}\tau^2}{2m}\right)^2}$$

$$\rho_0(\rho, z, \tau) = \rho\left(1 - \frac{U_n\tau}{r_1}\right)$$

$$z_0(\rho, z, \tau) = \left(z + \frac{q\,E_{\text{conv}}\tau^2}{2m}\right)\left(1 - \frac{U_n\tau}{r_1}\right) \tag{12}$$

One of the condition, necessary but not sufficient, to fulfil is $\forall \tau$, $(r_1(\rho, z, \tau) - r_c) > U_n\tau$, always true outside the wake.

Going beyond what was proposed in Vigren et al. (2015), who computed the mean velocity, we have calculated the first-order moment components of the ion distribution function:

$$\langle v_{\perp, \text{ion}} \rangle (\rho, z) = \frac{v_{\text{ion}} U_n}{n_{\text{ion}}(\rho, z)} \int_I \frac{\rho}{r_1} n_n(r_1)\, \mathrm{d}\tau \tag{13}$$

$$\langle v_{\parallel, \text{ion}} \rangle (\rho, z) =$$

$$\frac{v_{\text{ion}} U_n}{n_{\text{ion}}(\rho, z)} \int_I \left(U_n \frac{z + \frac{q E_{\text{conv}} \tau^2}{2m}}{r_1} - \frac{q E_{\text{conv}} \tau}{m} \right) n_n(r_1)\, \mathrm{d}\tau \tag{14}$$

and the second order ones as well.

In equation (14), we consider the initial velocity of the ion, term which has been neglected in the mean velocity relation provided by Vigren et al. (2015).

For a more comprehensive kinetic understanding, for each τ it corresponds only one 3-tuple in the velocity space at the position (ρ, z). This means that by integrating along τ, we integrate the distribution function along a 1D manifold in a 3D-velocity phase space.

2.2.2 Results from Model B

We present the different results from Model B and the different moments derived: the ion number density (2.2.2), the mean velocities (2.2.2), and the second-order centred moments (2.2.2). We have considered the same conditions as those assumed for Model A (see Table 1).

2.2.2.1 Zeroth-order moment. Fig. 3 (upper left-hand panel) depicts the ion number density, between 10^7 and 10^{10} m^{-3}. For the same conditions as for Model A (see Fig. 1) and the same position, the ion number density from Model B is significantly larger and exhibits a strong asymmetry with respect to $z = 0$ with larger values in $z < 0$.

The wake is clearly apparent: although Model B was built with a different 'philosophy' than Model A, this model highlights the same typical feature along the wake. Furthermore, Model B resolves much better the ion number density (i.e. suffers from less numerical instabilities) along this limit. A second boundary appears which corresponds to $\rho = r_c$ and $z < 0$. This boundary limits the region where ions are coming from $z > 0$ and the region where they cross the comet such that they are lost.

It is difficult to resolve well near the z-axis. In this region, the motion of ions is unidirectional (along the z-axis). For $z > 0$, the ions can come from below (not captured by the model) and above whereas for $z > 0$, they come only from above. Moreover, looking at the initial derivation, the volume element $V(t)$ shrinks here because $\sin \theta_0 = 0$

Finally, we have undertaken a parametric study for a full range of E_{conv} from 10^{-4} to 1 V m^{-1}: the ion number density is found to be proportional to $1/\sqrt{E_{\text{conv}}}$ (see Section 2.2.2.2).

2.1.2.2 First-order moments. Upper middle and right-hand panels in Fig. 3 show the mean velocities in both perpendicular and parallel directions.

Though the mean perpendicular velocity is to be bounded by U_n, the observed limit is lower: approximately ~ 550 m s^{-1}. An interesting feature is that the mean perpendicular velocity is constant along lines passing through the comet such that it is function of the angle with respect to the z-axis. Because of the strong drift driven

by the electric field, the main contribution to the ion number density comes from ions produced close. However, for $z < 0$, there is also a significant contribution from ions produced along the ρ-axis at $v_\rho = U_n$ (not possible for $z > 0$), which explains the asymmetry between $z > 0$ and $z < 0$.

Regarding the parallel velocity, even at a cometocentric of 20 km, ions are undergoing a strong acceleration and the mean velocity is going up to 10 km s^{-1} downward (along the direction of $\boldsymbol{E}_{\text{conv}}$) and $\langle v_\parallel \rangle \propto \sqrt{E_{\text{conv}}}$ derived from the parametric study. The conservation of mechanical energy yields:

$$v^2 = U_n^2 + \frac{2q E_{\text{conv}}}{m}(z_0 - z) \tag{15}$$

Assuming that the electric field is intense (so U_n is negligible) and the motion is only along z, we get for a given ion:

$$v_z \approx -\sqrt{\frac{2q E_{\text{conv}}}{m}(z_0 - z)} \propto \sqrt{E_{\text{conv}}} \tag{16}$$

Hence, the total mean velocity $\propto \sqrt{E_{\text{conv}}}$. In addition, in order to have the same flux for different E_{conv} (as this is not affecting the production term), the continuity equation implies $n_{\text{ion}} \propto 1/\sqrt{E_{\text{conv}}}$. This is in agreement not only with our simulations (see Section 2.2.2.1) but also with our analytical derivation from Vigren et al. (2015) (see Appendix G) outside the wake. Indeed, by considering the case $I = \mathbb{R}^+$ (i.e. $C_\tau = 1$ all the time in Vigren et al. 2015), true outside the wake, it is possible to derive an analytical relation for the ion number density and mean velocity proposed by Vigren et al. (2015). The result below is nevertheless slightly overestimated for the cases for which Vigren et al. (2015) consider $C_\tau = 0$. The full derivation is described in Appendix G, which yields the following relation for the ion number density:

$$n_{\text{ion}, V}(\rho, z) = \frac{v_{\text{ion}} Q}{8 U_n r} \sqrt{\frac{m}{q E_{\text{conv}}(r + z)}} \tag{17}$$

The calculation can be performed for the mean flux along z, i.e.:

$$n_{\text{ion}, V}(x, y, z)\langle v_\parallel \rangle_V = -\int_0^{+\infty} v_{\text{ion}} n_n \left(x, y, z + \frac{q E \tau^2}{2m} \right) \frac{q E \tau}{m}\, \mathrm{d}\tau$$

yielding:

$$n_{\text{ion}, V}\langle v_\parallel \rangle_V = -\frac{v_{\text{ion}} Q}{4\pi U_n \rho} \arccos\left(\frac{z}{r}\right) \quad \text{if } r \neq z, \rho \neq 0$$

$$= -\frac{v_{\text{ion}} Q}{4\pi U_n r} \quad \text{if } r = z, \rho = 0 \tag{18}$$

Thus, the mean parallel velocity is:

$$\langle v_\parallel \rangle_V = -\frac{2r}{\pi} \sqrt{\frac{q E_{\text{conv}}}{m(r - z)}} \arccos\left(\frac{z}{r}\right) \quad \text{if } r \neq z$$

$$= -\frac{2}{\pi} \sqrt{\frac{2q E_{\text{conv}} r}{m}} \quad \text{if } r = z \tag{19}$$

The ion-to-neutral ratio is then:

$$\frac{n_{\text{ion}, V}}{n_n} = \frac{v_{\text{ion}} \pi r}{2} \sqrt{\frac{m}{q E_{\text{conv}}(r + z)}} \tag{20}$$

which is independent of U_n as Vigren et al. (2015) neglected the initial newborn ion velocity. However, as mentioned in Section 2.2.2.1, the ion number density is expected to be $\propto 1/\sqrt{E_{\text{conv}}}$.

To prove that these analytical formula are correct outside the wake, we have plotted the ion number density from equation (17) (Fig. G1, left-hand panel), $n_{\text{ion, V}}/n_{\text{ion, H}}$ (to be compared with Fig. 3a

S832   *A. Beth and M. Galand*

Table 2. Characteristics from models A and B: name, dimensions in position and velocity, sampling in the velocity space, main assumption, computing (CPU) time, numerical inaccuracies, for a simulation of $20\,\text{km} \times 40\,\text{km}$ with a resolution of 100 m.

Model	Dimension (position × velocity)	Velocity sampling	Assumption	CPU time	Numerical inaccuracies
A	2 × 3	$50 \times 50 \times 50 = 125000$	σ_n	~ 500 h	Yes, within the wake continuity equation not fulfilled anywhere
B	2 × 1	500	$\sigma_n = 0$	<5 min	No (except maybe along the z-axis),continuity equation almost fulfilled everywhere except in some parts of the wake

from Vigren et al. ([2015](#), Fig. [G1](#), middle panel) and the mean ion velocity from equation (19) (Fig. [G1](#), right-hand panel).

E_{conv} in the denominator should not be misleading. In the model of Vigren et al. ([2015](#)), the acceleration can be 0. However, equation (20) is valid only outside the wake. For smaller and smaller E_{conv}, the wake moves away from the comet and the derivation cannot be applied close to it. A few simulations have been carried out to assess the effect of a lower and lower convective electric field. There is a surprising result: the model does not converge to the Haser model as intuitively expected for $E_{\text{conv}} \longrightarrow 0$, except in the area delimited in grey. Even for a negligible convective electric field but non null, as we are in the wake, $I = [0; \tau_1]\cup[\tau_2; +\infty[$. The integration over $[0; \tau_1]$ converges towards the Haser model. The integration over $[\tau_2; +\infty[$ (not taken into account in the delimited grey region) does not converge however towards 0: there is a competition between τ_2, increasing as E_{conv} decreases, and the integrand being more and more 'constant' ($r_1(\tau) \approx r$, i.e. independent of E_{conv}). In fact, our analytical derivation and the dependence on $\propto 1/\sqrt{E_{\text{conv}}}$ still hold even in the wake, except in the region delimited in grey.

Outside the wake, there is a perfect agreement between this analytical formula (Fig. [G1](#), left- and right-hand panels) and Model B (Fig. [3](#), upper left- and right-hand panels) for similar conditions. There are not strong discrepancies within the wake, except in the grey delimited region. $E_{\text{conv}} = 5 \times 10^{-4}\,\text{V m}^{-1}$ corresponds already to the case for which $\sqrt{2q E_{\text{conv}}\delta z/m} > U_n$, where δz is the difference in z between the production and final locations of the ion. The perpendicular velocity can be neglected with respect to U_n, even close to the comet.

2.1.2.3 Second-order moments. Lower panels in Fig. [3](#) show the mean standard deviation in two directions of the ion velocity. It is linked to the ion temperature and the departure of the σ_{max} direction from the electric field direction (see Appendix D).

Fig. [3](#) (lower left panel) represents the minimum standard deviation ranging from 0 to $200\,\text{m s}^{-1}$. There is a strong asymmetry between $z < 0$ and $z > 0$, for similar reasons to what was found for the perpendicular velocity (Section 2.2.2.2). By decreasing the range of available velocities for $z > 0$ (between 0 and $U_n\rho/r$), the minimum deviation (almost in the perpendicular direction) has to decrease as well. This explains why along the z-axis, the dispersion is ≈ 0 supporting the fact that the ion motion is reduced to 1D along this line.

Fig. [3](#) (lower middle panel) represents the maximum standard deviation. There is a huge dispersion up to $10\,000\,\text{m s}^{-1}$, of the same order of magnitude as the parallel velocity itself. The structure is similar to the ion number density (see Section 2.2.2.1) with an opposite behaviour: the parallel velocity dispersion and thus the parallel plasma temperature are increasing more and more outward. For $\sigma_{\text{max}} = 6\,\text{km s}^{-1}$, this represents a parallel ion temperature around ~ 6.5 eV, increasing approximatively with $\sim\rho$ for $z = 0$. This model shows that a constant temperature for ions is not a suitable assumption.

Finally, Fig. [3](#) (lower right panel) shows the deviation of the maximum dispersion direction with respect to the electric field direction. Our results show a very good alignment between both directions with a deviation within $\pm 3°$ outside the wake.

2.3 Comparisons between model a and model b

In this section, we confront Models A and B and draw the consequences for further and future modelling.

In Table [2](#), we list a few characteristics from both models. The difference in CPU time is not only explained by the additional dimension in Model A compared with Model B but also by the integration of the production term along the trajectory (about 100 points). The most convenient test for our simulations is the fulfilment of the continuity equation. For the fluid approach, this is one of the basic equations to solve. For the kinetic approach, this should be a consequence. Indeed, by integrating equation (A4) in the velocity space, we derive the continuity equation:

$$\nabla \cdot (n_{\text{ion}}\langle \boldsymbol{v}\rangle) = \nu_{\text{ion}}n_n(r), \qquad (21)$$

where n_{ion} and $\langle \boldsymbol{v}\rangle$ are the moments of order 0 and of order 1 of the ion distribution function. Numerically, we consider that the continuity equation is fulfilled if the relative difference between the left-hand and right-hand sides is less than a certain percentage (typically 10 per cent). Model A only gives us a few regions where it is fulfilled. For most of the computational domain, the left-hand side and the right-hand side are very different. This probably comes from the poor spatial resolution of the ion trajectory just at the surface of the comet: for example, for a given velocity, the first point that we sampled above the surface is at 100 m from the surface and for another velocity, the first point is at 200 m, instead of exactly just above the surface. This accumulation of inaccuracies in the production term (discontinuous at the surface) leads to underestimation of the ion number density from Model A. Moreover, the addition of integrations (2 more for Model A than for Model B) does not help for an accurate estimation.

Model B is more computationally efficient and more accurate, as illustrated in Table [2](#). The continuity equation is fulfilled within 1 per cent, except at the wake, in the transition region between $\rho = r_c$ and the wake boundary. Moreover, with its good accuracy and its agreement with other models (discussed in Section 3), despite additional assumptions (newborn ions only produced radially at one specific velocity U_n and travelling in a plane containing the z-axis), Model B and thus the initial work by Vigren et al. ([2015](#)), is a more relevant tool than Model A for the analysis of the interaction between the solar wind, its motional electric field and newborn cometary ions.

We would like to point out that for very small values of the convective electric field, Model B is constrained by computing inaccuracies which are:

(i) the boundaries of the subset I for the integration: the determination of $\tau_{\max}$, τ_1 and τ_2 are not exact and computationally expensive,

(ii) the upper limit of I – which can be $+\infty$ – has to be numerically finite and thus adjusted accordingly.

Indeed, the determination of I and its limits start to be difficult and less accurate for very small $E_{\text{conv}} < 10^{-6}$ V m^{-1}. This part can be computed aside with the appropriate software. $\tau_{\max}$, τ_1, and τ_2 are positive roots, if they exist, of the fourth-degree polynomial P_4:

$$P_4(\tau) = \left(\frac{q E_{\text{conv}}}{2m} \right)^2 \tau^4 + \left(\frac{z q E_{\text{conv}}}{m} - U_n^2 \right) \tau^2$$
$$- 2 U_n r_c \tau + \left(\rho^2 + z^2 - r_c^2 \right) \qquad (22)$$

P_4 has a maximum of two positive roots (Descartes' rule). Outside the wake, P_4 does not have positive roots. Inside the wake, it has two positive roots. By definition, the smallest positive root is $\tau_{\max}$ (or τ_1 depending on the region) and the highest positive one is τ_2. A priori, this is mathematically possible to give the analytical expression of these roots as the polynomial is of degree 4 (cf. Abel-Ruffini theorem and Ferrari's method). Such a formula would be cumbersome and beyond the scope of this paper. As E_{conv} decreases, because of the computing finite precision, the numerical roots become less and less accurate. However, a quantitative study shows that $\tau_1 \sim \frac{r - r_c}{U_n}$ and $\tau_2 \sim \frac{2m}{q E_{\text{conv}}} \sqrt{U_n^2 - \frac{z q E_{\text{conv}}}{m}}$ for $E_{\text{conv}} = o(1)$.

3 COMPARISONS WITH OTHER EXISTING WORKS

In this section, we compare the results from Model B with the Haser model (Section 3.1) and with other existing works on the convective electric field (Section 3.2).

3.1 General ion density model: the Haser (1957) model

3.1.1 Theory

Assuming a spherical symmetry for the production of neutrals at the surface of the comet, and neglecting the photo-dissociation or other chemical loss processes for neutrals, the neutral number density profile is given by equation (5) (Haser 1957) which is a realistic representation over the cometocentric distances considered here for a low outgassing comet.

The continuity equation applied to ions is reduced to:

$$\frac{1}{r^2} \frac{\mathrm{d}}{\mathrm{d}r} \left(n_{\text{ion}}(r) v(r) r^2 \right) = \nu_{\text{ion}} n_n(r) \qquad (23)$$

leading to:

$$n_{\text{ion}}(r) = \frac{Q}{4\pi \, v(r) r^2} \int_{r_c}^{r} \frac{\nu_{\text{ion}}(r')}{v(r')} \, \mathrm{d}r' \qquad (24)$$

For newborn ions, we assume a constant outflow velocity $v(r) = U_n$. The same formula is derived from Haser (1957) considering the ions as a daughter species and water as a parent species, with a characteristic length $L_d = U_n/\nu_{\text{ion}} \gg r$ for ions and infinite for neutrals.

Assuming that the coma is optically thin to EUV radiation ($\nu_{\text{ion}}(r) = $ constant), the ion number density is given by Galand et al. (2016):

$$n_{\text{ion,H}}(r) = \frac{\nu_{\text{ion}} Q}{4\pi U_n^2} \frac{r - r_c}{r^2} \qquad (25)$$
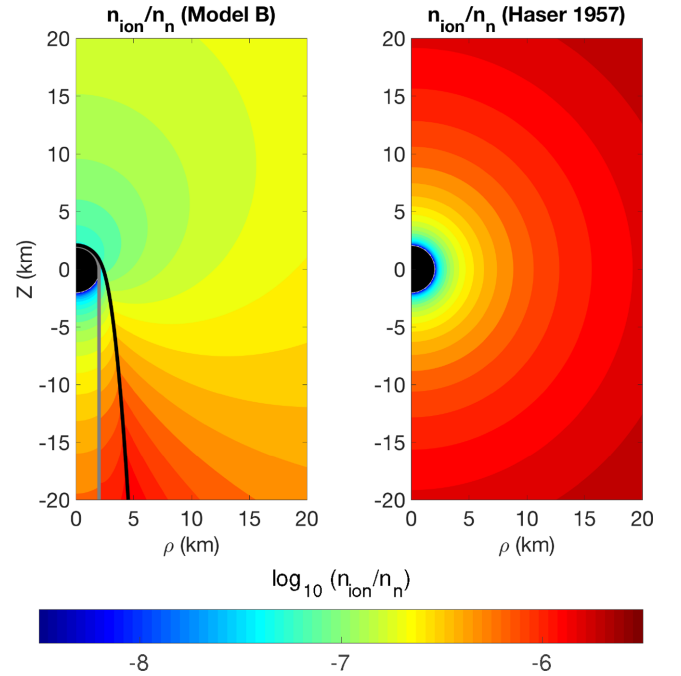

Figure 4. Plots of the ion number density over the neutral one for our Model B (left-hand panel) and for the Haser (1957) model (right-hand panel). The colour bar for the ratio is logarithmic.

and from equation (5), we derive that the ion-to-neutral or electron-to-neutral number density ratio is:

$$\frac{n_{\text{ion,H}}(r)}{n_n(r)} = \frac{\nu_{\text{ion}}}{U_n}(r - r_c) = \frac{r - r_c}{L_d} \qquad (26)$$

where L_d is the length scale. The mean ion velocity is:

$$\langle \boldsymbol{v}_{\text{ion,H}} \rangle = U_n \boldsymbol{e}_r = \underbrace{U_n \frac{\rho}{r} \, \boldsymbol{e}_\rho}_{\langle v_\perp \rangle} + \underbrace{U_n \frac{z}{r} \, \boldsymbol{e}_z}_{\langle v_\parallel \rangle} \qquad (27)$$

This model is used as a reference for comparison because it represents the case where there is no electric field and ions are not undergoing any acceleration along their trajectory.

3.1.2 Comparison with Model A and Model B

Fig. 4 shows a comparison of n_{ion}/n_n between our Model B (section 2.2) and the Haser (1957) model (Section 3.1.1).

The presence of the solar wind convective electric field tends to decrease the ion number density. If the right-hand side of equation (23) and the spherical symmetry remain unchanged, as the force accelerates the ions, the ion number density should decrease to ensure flux conservation. At a given location, the ion-to-neutral number density ratio should thus be higher for the Haser model than for Model B. One exception is close to the comet's surface, for $z > 0$: the newborn ions from the surface facing the electric field are first decelerated so that $v < U_n$ during a short time before reaching the maximum z in their trajectory and then accelerating by $\boldsymbol{E}_{\text{conv}}$. Moreover, even produced far away, newborn ions close to the z-axis ($z > 0$) are strongly deflected and reach the comet. As seen in Fig. 4, the ion-to-neutral number density ratio is higher for Model B than for the Haser model, only in a few kilometres in the $z > 0$ direction.
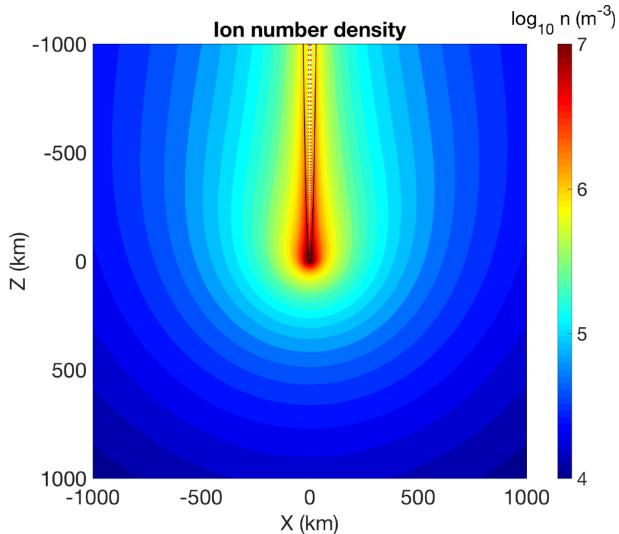
Ion number density

Figure 5. Ion number density from Model B in logscale for the same conditions as Madanian et al. (2016): $Q = 10^{26}\,\text{s}^{-1}$, $U_n = 1000\,\text{m s}^{-1}$, $\nu_{\text{ion}} = 10^{-7}\,\text{s}^{-1}$, $E_{\text{conv}} = 5.10^{-4}\,\text{V m}^{-1}$ (listed by (+) in Table 1). The contours are symmetrical with respect to the z-axis and reversed to be consistent with their paper.

3.2 Comparison with other models which include the motional electric field

Two main studies on the solar wind motional electric field have been published by Vigren et al. (2015) and Madanian et al. (2016). In Section 2.2, we detailed how we have improved and extended the work by Vigren et al. (2015). We propose here to compare our results (here Model B) with the work from Madanian et al. (2016).

Madanian et al. (2016) investigated the ion number density up to 1000 km from the comet using a test particle model for conditions encountered at 3 au. Their model takes into account: the photo-ionization by solar radiation, the charge exchange with solar-wind protons, the interplanetary magnetic field, and the motional electric field. However, the ambipolar electric field is not included as this caused instability in their model.

In order to compare our findings with those from Madanian et al. (2016), we carried out a run with Model B (see Section 2.2) under the same conditions as those chosen by Madanian et al. (2016) (see Table 1). The derived ion number density is shown in Fig. 5. There is a very good agreement with fig. 9 of Madanian et al. (2016). The main departure is a little drift of the ion tail to the left ($x < 0$) far from the comet, not seen in the results from Model B. At 1000 km, the effect of the ion gyration – included in Madanian et al. (2016) – starts to become important: the ions are first drifting due to $\boldsymbol{E}_{\text{conv}}$ and then picked up by the solar wind coming from the right ($x > 0$). However, even at 1000 km, the gyroradius remains large in the solar wind frame and the deflection remains small.

Nevertheless, by its simplicity and its computing time (a few minutes CPU time), Model B catches the global behaviour with good accuracy of the ion distribution by comparison to the test particle model from Madanian et al. (2016).

4 CONCLUSION

In this paper, we investigate the effect of the convective electric field on the dynamic of newborn cometary ions based on different kinetic models for a low cometary activity. In such a case, the solar wind can penetrate the coma, carrying itself the convective electric field E_{conv}. We show that such a convective electric field changes the ion number density profile, to a radial $r^{-3/2}$ dependency, instead of the observed $1/r$ decrease. We highlight that there is also a dependency with respect to the convective electric field direction and its intensity; asymptotically, for a strong convective electric field, the ion number density is proportional to $1/\sqrt{E_{\text{conv}}}$. Thus, including only its effect cannot explain the plasma density observations at large heliocentric distances.

In reality, the convective electric field does not act alone but is combined with the ambipolar electric field which counteracts its effect. Indeed, in order to ensure the quasi-neutrality of the plasma, the ambipolar electric field is set up to prevent electrons from escaping the cometary ionosphere. Further investigations should be carried out to assess the combined effect of both electric fields on the cometary ionosphere. For instance, the kinetic modelling of the coma, solving the Vlasov–Maxwell equations through a particle-in-cell approach as presented by Deca et al. (2017), could improve our understanding in such a situation.

REFERENCES

Altwegg K. et al., 1993, A&A, 279, 260
Balsiger H. et al., 1986, Nature, 321, 330
Balsiger H. et al., 2007, Space Sci. Rev., 128, 745
Behar E., Nilsson H., Wieser G. S., Nemeth Z., Broiles T. W., Richter I., 2016, Geophys. Res. Lett., 43, 1411
Benna M., Mahaffy P. R., 2006, Geophys. Res. Lett., 33, n/a
Beth A. et al., 2016, MNRAS, 462, S562
Bieler A. et al., 2015, Nature, 526, 678
Broiles T. W. et al., 2015, A&A, 583, A21
Broiles T. W. et al., 2016, J. Geophys. Res. Space Phys., 121, 7407
Burch J. L., Goldstein R., Cravens T. E., Gibson W. C., Lundin R. N., Pollock C. J., Winningham J. D., Young D. T., 2007, Space Sci. Rev., 128, 697
Churyumov K. I., Gerasimenko S. I., 1972, in Chebotarev G. A., Kazimirchak-Polonskaia E. I., Marsden B. G., eds, Proc. IAU Symp. 45, The Motion, Evolution of Orbits, and Origin of Comets. Reidel, Dordrecht, p. 27
Cravens T. E., 1987, Adv. Space Res., 7, 147
Deca J., Divin A., Henri P., Eriksson A., Markidis S., Olshevsky V., Horányi M., 2017, Phys. Rev. Lett., 118, 205101
Edberg N. J. T. et al., 2015, Geophys. Res. Lett., 42, 4263
Eriksson A. I. et al., 2007, Space Sci. Rev., 128, 729
Eriksson A. I. et al., 2017, A&A, 605, A15
Fougere N. et al., 2016, A&A, 588, A134
Fuselier S. A. et al., 2015, A&A, 583, A2
Fuselier S. A. et al., 2016, MNRAS, 462, S67
Galand M. et al., 2016, MNRAS, 462, S331
Glassmeier K.-H., 2017, Philosophical Transactions of the Royal Society of London A: Mathematical, Physical and Engineering Sciences, 375
Glassmeier K.-H., Boehnhardt H., Koschny D., Kührt E., Richter I., 2007, Space Sci. Rev., 128, 1
Goetz C. et al., 2016a, MNRAS, 462, S459
Goetz C. et al., 2016b, A&A, 588, A24
Hanner M. et al., 1985, Icarus, 64, 11

Hansen K. C. et al., 2007, Space Sc. Rev., 128, 133
Hansen K. C. et al., 2016, MNRAS, 462, S491
Haser L., 1957, Bull. Soc. Roy. Sci. Liège, 43, 740
Hässig M. et al., 2015, Science, 347, aaa0276
Heritier K. L. et al., 2017a, MNRAS, 469, S118
Heritier K. L. et al., 2017b, MNRAS, 469, S427
Ip W.-H., 2004, Global solar wind interaction and ionospheric dynamics. pp 605
Ip W.-H., Axford W. I., 1987, Nature, 325, 418
Lamy P. L., Toth I., Davidsson B. J. R., Groussin O., Gutiérrez P., Jorda L., Kaasalainen M., Lowry S. C., 2007, Space Sci. Rev., 128, 23
Madanian H. et al., 2016, J. Geophys. Res. Space Phys., 121, 5815
Madanian H. et al., 2017, AJ, 153, 30
Mandt K. E. et al., 2016, MNRAS, in press
Nemeth Z. et al., 2016, MNRAS, 462, S415
Neubauer F. M. et al., 1986, Nature, 321, 352
Nilsson H. et al., 2007, Space Sci. Rev., 128, 671
Nilsson H. et al., 2015a, Science, 347, aaa0571
Nilsson H. et al., 2015b, A&A, 583, A20
Odelstad E. et al., 2015, Geophys. Res. Lett., 42, 10,126
Reinhard R., 1986, Nature, 321, 313
Tenishev V., Combi M., Davidsson B., 2008, ApJ, 685, 659
Tuckerman M. E., Mundy C. J., Martyna G. J., 1999, EPL (Europhys. Lett.), 45, 149
Tuckerman M. E., Liu Y., Ciccotti G., Martyna G. J., 2001, J. Chem. Phys., 115, 1678
Vigren E., Eriksson A. I., 2017, AJ, 153, 150
Vigren E., Galand M., Eriksson A. I., Edberg N. J. T., Odelstad E., Schwartz S. J., 2015, ApJ, 812, 54
Vigren E. et al., 2016, AJ, 152, 59
Wurz P. et al., 2015, A&A, 583, A22

APPENDIX A: DISCUSSION ABOUT THE BOLTZMANN EQUATION

We have introduced in equation (3) a factor depending on the geometry and the coordinates used for the representation of the distribution function. This factor plays a key role according to the set of coordinates used for the resolution of the Boltzmann equation. We strongly invite the reader to look at Tuckerman, Mundy & Martyna (1999) and Tuckerman et al. (2001) dealing with non-Hamiltonian systems. By not using the conjugate momenta of the space coordinates, we might introduce a mistake into the distribution function. Even for a non-Hamiltonian system, Liouville theorem $df/dt = 0$ stands but – and we strongly insist on that point – the measure $d^6 x^i$, the infinitesimal volume element – product of differentials of each variable x_i of the distribution function f – is not necessarily conserved in the 6D phase space along the trajectory.

Consider a non-Hamiltonian system:

$$\dot{x}^i = \xi^i(x^i, t)$$

for the evolution of the i coordinate $x = x^1, \dots, x^6$ with initial values $x_0 = x_0^1, \dots, x_0^n$. At time t, the coordinates are:

$$x_t = x_t(t; x_0^1, \dots, x_0^n)$$

Now, we define the Jacobian J of the transformation between x_0 and x_t:

$$J(x_t; x_0) = \frac{\partial(x^1, \dots, x^n)}{\partial(x_0^1, \dots, x_0^n)} = \det M = \exp(\mathrm{Tr}(\log(M))) \quad (A1)$$

with

$$M_{i,j} = \frac{\partial x_t^i}{\partial x_0^j}$$

It is possible to show that:

$$\frac{dJ}{dt} = J \sum_i \left(\frac{\partial \xi^i}{\partial x^i} \right) = J \kappa(x_t). \quad (A2)$$

The term $\kappa = \sum_i \partial \xi^i / \partial x^i$ represents the compressibility of the coordinates. The system of coordinates as defined in Hamiltonian mechanics (known as canonical coordinates) is incompressible by definition, which is not the case of ours (no canonical). Let's consider the cylindrical coordinate case, i.e. (ρ, φ, z) coordinates. Their associated conjugate momenta are defined as:

$$p_\rho = m\dot{\rho} = m v_\rho$$

$$p_\varphi = m\rho^2 \dot{\varphi} = m\rho v_\varphi$$

$$p_z = m\dot{z} = m v_z$$

and from Hamiltonian equations

$$\frac{\partial \dot{\rho}}{\partial \rho} + \frac{\partial \dot{\varphi}}{\partial \varphi} + \frac{\partial \dot{z}}{\partial z} + \frac{\partial \dot{p}_\rho}{\partial p_\rho} + \frac{\partial \dot{p}_\varphi}{\partial p_\varphi} + \frac{\partial \dot{p}_z}{\partial p_z} = 0. \quad (A3)$$

During the motion, the volume element $dV_C = d\rho \, d\varphi \, dz \, dp_\rho \, dp_\varphi \, dp_z$ in the 6D phase space stays unchanged (equation A3). $(\rho, \varphi, z, p_\rho, p_\varphi, p_z)$ is a canonical set of coordinates. However, if we use the volume element $dV_{NC} = d\rho \, d\varphi \, dz \, dv_\rho \, dv_\varphi \, dv_z$ rather than dV_C, by the change of coordinates, we have $dV_C = m^3 \rho \, dV_{NC}$. $(\rho, \varphi, z, v_\rho, v_\varphi, v_z)$ is a non-canonical set of coordinates.

Let's consider now particles produced with the distribution function $f(\rho_0, \varphi_0, z_0, p_\rho, p_\varphi, p_z)$ at (ρ_0, φ_0, z_0) and propagating to another location (ρ_t, φ_t, z_t). Applying the Liouville theorem, undergoing conservative forces and Hamiltonian coordinates:

$$f(\rho_0, \varphi_0, z_0, p_{\rho_0}, p_{\varphi_0}, p_{z_0}) = f(\rho_t, \varphi_t, z_t, p_{\rho_t}, p_{\varphi_t}, p_{z_t})$$

$$f(\rho_0, \varphi_0, z_0, p_{\rho_0}, p_{\varphi_0}, p_{z_0}) \, dV_0 = f(\rho_t, \varphi_t, z_t, p_{\rho_t}, p_{\varphi_t}, p_{z_t}) \, dV_0$$

The reader should remember that the Liouville theorem is a Hamiltonian mechanics theorem such that the incompressibility of the coordinates is assumed. Therefore, the number of particles is conserved along the trajectory. However, if we consider the volume element dV_{NC}:

$$f(\rho_0, \varphi_0, z_0, v_{\rho_0}, v_{\varphi_0}, v_{z_0}) \, dV_{NC}(t)$$
$$= f(\rho_t, \varphi_t, z_t, v_{\rho_t}, v_{\varphi_t}, v_{z_t}) \, dV_{NC}(0)$$

$$\rho_0 f(\rho_0, \varphi_0, z_0, v_{\rho_0}, v_{\varphi_0}, v_{z_0}) \, dV_C = \rho_t f(\rho_t, \varphi_t, z_t, v_{\rho_t}, v_{\varphi_t}, v_{z_t}) \, dV_C$$

and thus

$$\rho_0 f(\rho_0, \varphi_0, z_0, v_{\rho_0}, v_{\varphi_0}, v_{z_0}) = \rho_t f(\rho_t, \varphi_t, z_t, v_{\rho_t}, v_{\varphi_t}, v_{z_t})$$

Depending on the coordinates in which the distribution is described (Hamiltonian or not, canonical coordinates or not), a corrective factor has to be applied to take into account the compressibility of the coordinates in the 6D phase space.

For a more general application, we have to define $\kappa = \dot{w}$ ($\dot{\rho}/\rho$ for our example). Thus, from equation (A2), the Jacobian J can be written as:

$$J = \exp(w(x_t) - w(x_0))$$

By using $(\rho, \varphi, z, v_\rho, v_\varphi, v_z)$ instead of the conjugate momenta, the volume $dV_1(t)$ following the particles is not constant along the

trajectory. However, we have:

$$\exp(-w(x_t))\, dV_{NC}(t) = \exp(-w(x_0))\, dV_{NC}(0)$$

or

$$dV_{NC}(t) = \exp(w(x_t) - w(x_0))\, dV_{NC}(0)$$

with $\exp(-w(x_t)) = \rho_t$ (for our case) and $\exp(-w(x_0)) = \rho_0$ (where the ion is produced), due to the cylindrical symmetry in 3D space and the use of velocities instead of conjugate momenta. This is exactly the factor we get for the transformation between (x, y, z, v_x, v_y, v_z), a Cartesian-like 6D frame and thus incompressible, and $(\rho, \varphi, z, v_\rho, v_\varphi, v_z)$.

More generally, $\exp(-w(x_t)) = \sqrt{g}$, where $\sqrt{g}$ is the metric determinant factor defined by our system of coordinates. For Hamiltonian mechanics, $\sqrt{g} = 1$ (canonical coordinates) and the 6D volume element do not change along the trajectory so that the distribution function does not change in collisionless problems (cf. Liouville theorem). For non-Hamiltonian cases, the Liouville equation is given by (Tuckerman et al. 2001):

$$\frac{\partial(f\sqrt{g})}{\partial t} + \sum_k \frac{\partial(f\sqrt{g}\xi^k)}{\partial x^k} = 0. \tag{A4}$$

The Liouville equation still holds ($df/dt = 0$). However, the average of any property A, such as the moments, has to be determined from the distribution function f and the invariant measure $\sqrt{g}\, dx^k$:

$$\langle A \rangle = \frac{\int A(x^k) f(x^k) \sqrt{g(x^k)}\, dx^k}{\int f(x^k) \sqrt{g(x^k)}\, dx^k}.$$

The invariant measure has to be considered to derive the continuity equation from the Boltzmann equation in cylindrical symmetry ($\sqrt{g} = \rho$) or spherical symmetry ($\sqrt{g} = r^2$) for position-velocity coordinates which are not canonical, unlike position-momentum ones.

For these reasons, we have introduced ρ_0/ρ (geometry and not canonical coordinates) in equation (6) and further in this paper to take into account such a 'metric' effect.

APPENDIX B: PARABOLA PARAMETRIZATION

In general, particle trajectories are expressed either as a function of time $\boldsymbol{r} = (x(t), y(t), z(t))$ or through a relation between position coordinates. For a particle undergoing a constant acceleration in one direction – as it is the case here for the electric field – its trajectory describes a parabola. The newborn ion trajectory is a parabola in the plane perpendicular to $\boldsymbol{E}_{conv} \times \boldsymbol{v}$, passing through the position where it is observed (see Fig. B1). We propose here to parametrize the parabola in cylindrical polar coordinates (ρ, φ, z) with respect to its focus, where the z-axis is along $-\boldsymbol{E}_{conv}$(see Fig. B1), $\parallel$ and $\perp$ refer to directions parallel and perpendicular to $\boldsymbol{E}_{conv}$ (or z-axis), respectively.

We choose the position $A = (x, 0, z)_{cartesian} = (\rho, 0, z)_{cylindrical}$ and velocity (v_ρ, v_φ, v_z). The parabola in the plane $(\boldsymbol{E}_{conv}, \boldsymbol{v})$ is characterized by its semilatus rectum p and the position of its focus, F. p is given by:

$$p = \frac{m(v_\rho^2 + v_\varphi^2)}{q E_{conv}} = \frac{mv_\perp^2}{q E_{conv}} \tag{B1}$$

constant during the motion, as $v_\perp$ is a constant of the motion. We need also to derive the relative position of the focus F of the parabola
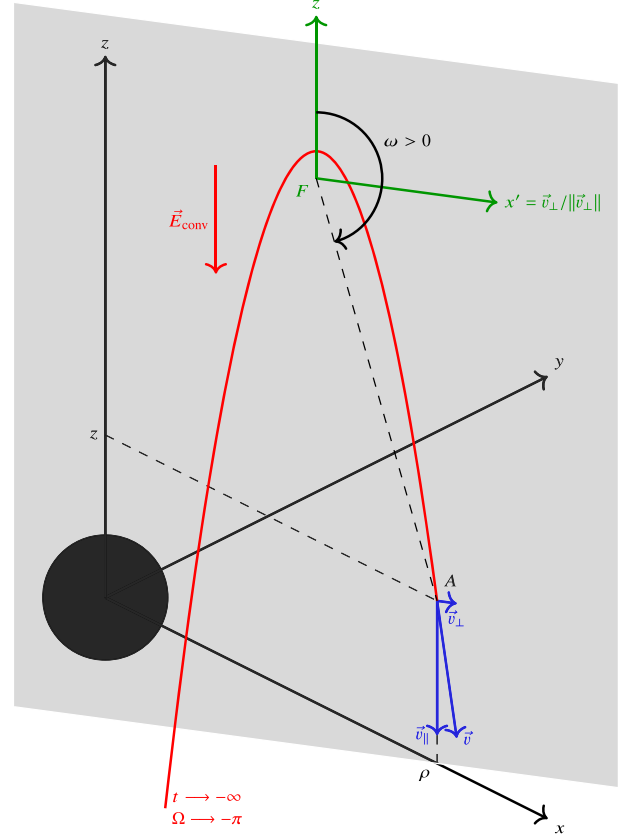

Figure B1. Schematic of the ion trajectory and the different considered frames. The black frame is the frame centred on the comet with the ion in the *Oxz* plane. The blue arrows represent the ion velocity and its projection. The green frame represents the normalized frame with respect to the projected velocities and centred on the focus of the parabola *F*. *A* refers to the point of observation through which ions are going through and the moments are derived.

with respect to the final position A:

$$\boldsymbol{AF} = -\frac{m\boldsymbol{v}_\parallel \cdot \boldsymbol{E}_{conv}}{q E_{conv}^2}\boldsymbol{v}_\perp + \frac{m(v_\parallel^2 - v_\perp^2)}{2q E_{conv}}\boldsymbol{e}_z$$

$$= \frac{mv_\parallel v_\perp}{q E_{conv}}\boldsymbol{e}_{x'} + \frac{m(v_\parallel^2 - v_\perp^2)}{2q E_{conv}}\boldsymbol{e}_z \tag{B2}$$

By definition, the frame $Ox'z$ is oriented such that $v_\perp$ is positive (see Fig. B1). In the original frame, the parametrization of an ion trajectory, with respect to Ω, is then given by:

$$x = \frac{v_\rho}{v_\perp}\left(\frac{p\sin\Omega}{1 + \cos\Omega} + \frac{mv_\perp v_\parallel}{qE}\right) + \rho \tag{B3}$$

$$y = \frac{v_\varphi}{v_\perp}\left(\frac{p\sin\Omega}{1 + \cos\Omega} + \frac{mv_\perp v_\parallel}{qE}\right) \tag{B4}$$

$$z = \left(\frac{p\cos\Omega}{1 + \cos\Omega} + \frac{m(v_\parallel^2 - v_\perp^2)}{2qE}\right) + z \tag{B5}$$

with $v_\parallel = \boldsymbol{v}.\boldsymbol{e}_z$ and $v_\perp = \|\boldsymbol{v} - \boldsymbol{v}_\parallel\|$, the initial parallel and perpendicular velocities and $\Omega \in\,] -\pi\,;\omega]$, ω is the value of Ω for which the ion is at A:

$$\omega = -2\arcsin\left(\frac{v_\parallel}{v}\right) \tag{B6}$$

The last relation to determine is the one between the time t, s, and Ω or between dt, ds, and dΩ. Let's call R, the distance between the ion and the focus F given by:

$$R(\Omega) = \frac{p}{1 + \cos \Omega} \tag{B7}$$

Thus:

$$
\begin{aligned}
\mathrm{d}s &= \sqrt{\mathrm{d}R^2 + (R\mathrm{d}\Omega)^2} \\
&= \sqrt{\frac{2p^2}{(1 + \cos \Omega)^3}} \, \mathrm{d}\Omega \\
&= R(\Omega)\sqrt{\frac{2}{1 + \cos \Omega}} \, \mathrm{d}\Omega \\
&= \frac{R(\Omega)}{\cos\left(\frac{\Omega}{2}\right)} \, \mathrm{d}\Omega
\end{aligned}
\tag{B8}
$$

However, we need also to express the ion velocity. Based on the conservation of the mechanical energy:

$$
\begin{aligned}
v^2 &= v_\perp^2 + \frac{2qE_{\mathrm{conv}}}{m}\left(\frac{p}{2} - \frac{p\cos\Omega}{1 + \cos\Omega}\right) \\
&= v_\perp^2 + \frac{qpE_{\mathrm{conv}}}{m}\frac{1 - \cos\Omega}{1 + \cos\Omega} \\
&= v_\perp^2 + \frac{qpE_{\mathrm{conv}}}{m}\tan^2\left(\frac{\Omega}{2}\right) \\
&= \frac{v_\perp^2}{\cos^2\left(\frac{\Omega}{2}\right)} \quad \text{(from equation B1)}
\end{aligned}
\tag{B9}
$$

leading to:

$$\mathrm{d}t = \frac{\mathrm{d}s}{v} = \frac{R(\Omega)}{v_\perp} \, \mathrm{d}\Omega \tag{B10}$$

Therefore, from equations (B1), (B7), and (B10), equation (6) becomes:

$$f(\boldsymbol{r}, \boldsymbol{v}) = \frac{mv_\perp}{qE_{\mathrm{conv}}}\int_{-\pi}^{\omega} \frac{P_{\mathrm{ion}}(\boldsymbol{r}_0(\Omega), \boldsymbol{v}_0(\Omega))}{1 + \cos\Omega}\frac{\rho_0(\Omega)}{\rho} \, \mathrm{d}\Omega \tag{B11}$$

This parametrization is more usable than equation (6), as the boundaries of integration are finite and easily known according to the initial conditions.

APPENDIX C: NUMERICAL EVALUATION OF THE DISTRIBUTION FUNCTION (SUPPLEMENTARY INFORMATION)

We integrate numerically equation (7) using the Gauss–Legendre quadrature whose accuracy and order are linked to the number of considered points for the integration: for N^L points, the method is of the order $2N^L - 1$. Moreover, the Gauss–Legendre method is adapted for numerical integration with finite lower and upper boundaries. For the integration I between a and b of a given function f, the numerical value is given by:

$$\int_a^b f(x)\,\mathrm{d}x \approx \sum_{i=1}^{N^L} f(x_i)w_i^L \tag{C1}$$

where $x_i = \frac{a+b}{2} + r_i^L\frac{b-a}{2}$, r_i^L are the roots for the Legendre polynomials of degree N^L and w_i^L, the associated weights. Their values are computed from the Numerical Recipes. Typically, we choose $N^L = 100$.

One of the numerical issues for this computation is the presence of the comet: some parabolas cross the comet. In that case, the production term is set to 0 within the comet and any ion crossing the comet is lost except those leaving the cometary surface and above. This leads to discontinuities in the distribution function in the velocity space.

For the determination of the different moments of interest, we use another numerical approach, the Gauss-Hermite quadrature:

$$
\begin{aligned}
\int_{-\infty}^{+\infty} g(x)\,\mathrm{d}x &= \int_{-\infty}^{+\infty} h(x)e^{-x^2}\,\mathrm{d}x \\
&\approx \sum_{i=1}^{N^H} h(r_i)w_i^H \approx \sum_{i=1}^{N^H} g(r_i)e^{(r_i^H)^2}w_i^H
\end{aligned}
\tag{C2}
$$

where r_i^H are the roots for the Hermite polynomials of degree N^H and w_i^H, the associated weights. This is particularly adapted to the integration of functions whose shapes are close to a normal (i.e. Maxwellian) distribution and with infinite lower and upper boundaries. Typically, we choose $N^H = 50$, which means we use $125\,000$ points in the velocity space for sampling. The method is adapted to be applied to 3D with different dispersions.

$$
\begin{aligned}
\int_{-\infty}^{+\infty} f(\boldsymbol{r}, \boldsymbol{v})\,\mathrm{d}^3\boldsymbol{v} &\approx \sum_{i=1}^{N^H}\sum_{j=1}^{N^H}\sum_{k=1}^{N^H} f(\boldsymbol{r}, v_i, v_j, v_k)W_iW_jW_k \\
v_i &= \sqrt{2\alpha^2}r_i^H + V_{x0}, \quad W_i = \sqrt{2}e^{(r_i^H)^2}w_i^H \\
v_j &= \sqrt{2\beta^2}r_j^H + V_{y0}, \quad W_j = \sqrt{2}e^{(r_j^H)^2}w_j^H \\
v_k &= \sqrt{2\gamma^2}r_k^H + V_{z0}, \quad W_k = \sqrt{2}e^{(r_k^H)^2}w_k^H
\end{aligned}
\tag{C3}
$$

where α, β, γ, V_{x0}, V_{y0}, and V_{z0} are unknown and flexible: they fix the points in the velocity space where the distribution function should be evaluated. We have to optimize these parameters to sample in the wisest and the most efficient way f, i.e. minimizing the error. To overcome this issue, we calculate recursively the moments:

(i) We start the computation with $\alpha = \beta = \gamma = U_n$ and $V_{x0} = V_{y0} = V_{z0} = 0$, we compute the moments, n, $\langle v_x \rangle$, $\langle v_y \rangle$ $\langle v_z \rangle$, $\langle v_x^2 \rangle$, $\langle v_y^2 \rangle$, $\langle v_z^2 \rangle$,

(ii) At step 1, the moments provide the density n_1, the mean velocity $\langle \boldsymbol{v}_1 \rangle$, and also the second-order centred moments. These values are used as inputs to compute new values for v_i, v_j, and v_k, adapting the grid and sampling the distribution as wise as possible. For the next step, the initial inputs are readjusted:

$V_{x0} = \langle v_x \rangle$, $V_{y0} = \langle v_y \rangle$, $V_{z0} = \langle v_z \rangle$, $\alpha = \sigma_x = \sqrt{\langle v_x^2 \rangle - \langle v_x \rangle^2}$, $\beta = \sigma_y = \sqrt{\langle v_y^2 \rangle - \langle v_y \rangle^2}$, $\gamma = \sqrt{\langle v_z^2 \rangle - \langle v_z \rangle^2}$,

(iii) We repeat the process until the density converges with a certain tolerance.

This approach is useful as we are presuming nothing about the different moments of the distribution function, but only what the shape of the bulk is: we assume that it is a 3D-Maxwellian distribution.

APPENDIX D: STANDARD AND ANGULAR DEVIATIONS

We would like to confirm whether the distribution function is aligned with the electric field or not. If we assume a 2D-Maxwellian distribution, there are two directions over which two dispersions have to be maximized/minimized, as illustrated in Fig. D1. For our 3D
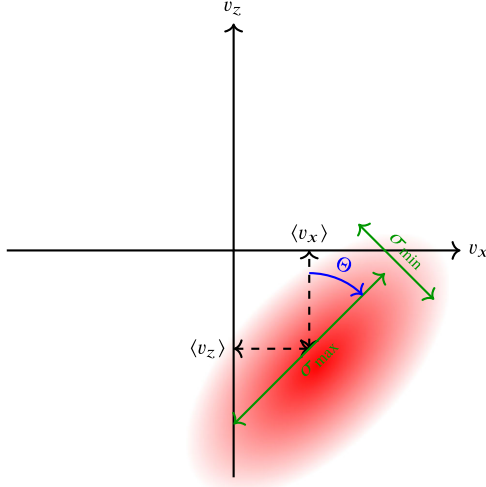
Figure D1. Schematic representation of the distribution function, displayed in red, with the first- and second-order moments. Θ here is negative and has been exaggerated – not reflecting our simulations for the benefit of the visualization -.

case, this requires the determination of the eigenvalues and associated eigenvectors of the covariance matrix (see equation 8):

$$\mathbf{M} = \begin{pmatrix} \sigma_x^2 & \sigma_{xy} & \sigma_{xz} \\ \sigma_{xy} & \sigma_y^2 & \sigma_{yz} \\ \sigma_{xz} & \sigma_{yz} & \sigma_z^2 \end{pmatrix} = \begin{pmatrix} \sigma_x^2 & 0 & \sigma_{xz} \\ 0 & \sigma_y^2 & 0 \\ \sigma_{xz} & 0 & \sigma_z^2 \end{pmatrix} \qquad (D1)$$

A straightforward eigenvalue is σ_y^2 because of the cylindrical symmetry. The problem can be reduced by studying the matrix:

$$\mathbf{N} = \begin{pmatrix} \sigma_x^2 & \sigma_{xz} \\ \sigma_{xz} & \sigma_z^2 \end{pmatrix} \qquad (D2)$$

As the trace $\text{Tr}(N) > 0$ and the determinant $\det(N) > 0$ (see Cauchy–Schwarz inequality), the eigenvalues are positive and are defined as $\sigma_{\max}^2$ and $\sigma_{\min}^2$, where $\sigma_{\max}^2 > \sigma_{\min}^2$. Analytically, the eigenvalues are given by:

$$\sigma_{\max}^2 = \frac{\sigma_x^2 + \sigma_z^2}{2} + \frac{\sqrt{(\sigma_x^2 - \sigma_z^2)^2 + 4\sigma_{xz}^2}}{2}$$

$$\sigma_{\min}^2 = \frac{\sigma_x^2 + \sigma_z^2}{2} - \frac{\sqrt{(\sigma_x^2 - \sigma_z^2)^2 + 4\sigma_{xz}^2}}{2} \qquad (D3)$$

and then the deviation of the main direction of the distribution (direction for $\sigma_{\max}$) from the electric field direction is given by:

$$\Theta = -\arctan\left(\frac{\sigma_x^2 - \sigma_{\min}^2}{\sigma_{xy}}\right), \sigma_{xy} \neq 0 \qquad (D4)$$

related to the direction of the eigenvectors. Indeed, if $\sigma_{xy} = 0$, σ_{xx} is either $\sigma_{\min}$ ($\Theta = 0$) or $\sigma_{\max}$ ($\Theta = \pi/2$), as shown in Fig. D1.

APPENDIX E: THE COMETARY WAKE

As detailed in Section 2.1, our simulations and previous works (e.g. Vigren et al. 2015) bring to light the presence of a cometary wake induced by the comet itself. The wake delimits the region where the ion number density undergoes a discontinuity: this limit is the upper limit in the z direction that ions born at the surface can reach. In this Appendix, we propose a detailed demonstration to determine this boundary.

Considering the motion of ions in the (ρ, z) plane, their trajectories are given by:

$$\rho(t) = \rho_0 + v_{\rho 0} t$$

$$z(t) = z_0 + v_{z0} t - \frac{q E_{\text{conv}}}{2m} t^2 \qquad (E1)$$

For the ions which have been just produced on the comet's surface, at the distance r_c from the comet's centre and at a radial velocity U_n, we get:

$$\rho(t) = (r_c + U_n t) \sin\theta_0$$

$$z(t) = (r_c + U_n t) \cos\theta_0 - \frac{q E_{\text{conv}}}{2m} t^2 \qquad (E2)$$

where θ_0 is the initial colatitude of the ion at the surface with respect to the z-axis.

The wake is defined by the maximum $z(t)$, which an ion can have at a given $\rho(t)$. With the current set of equations, the problem is that for a given t, all the ions have not the same ρ such that we need to express z as a function of ρ (and θ_0). equation (E2) implies:

$$z(\rho, \theta_0) = \frac{\rho}{\tan\theta_0} - \frac{q E_{\text{conv}}}{2m U_n^2} \left(\frac{\rho}{\sin\theta_0} - r_c\right)^2 \qquad (E3)$$

The position of the wake boundary is then defined by the maximum value $z(\rho, \vartheta)$ for a fixed ρ and $\vartheta \in [0, \pi]$, such that:

$$\left(\frac{\partial z}{\partial\theta_0}\right)_\rho (\rho, \vartheta) = 0$$

$$= -\frac{\rho}{\sin^2\vartheta} \left[1 - \frac{q E_{\text{conv}} r_c}{m U_n^2} \left(\frac{\rho}{r_c \sin\vartheta} - 1\right) \cos\vartheta\right] \qquad (E4)$$

ϑ is the solution of this transcendental equation. However, some simplifications can be made:

$$1 - \frac{q E_{\text{conv}} r_c}{m U_n^2} \left(\frac{\rho}{r_c \sin\vartheta} - 1\right) \cos\vartheta = 0$$

$$\left(\frac{\rho}{r_c} - \sin\vartheta\right) \cos\vartheta = \frac{m U_n^2}{q E_{\text{conv}} r_c} \sin\vartheta$$

$$\left(\frac{\rho}{r_c} - \sin\vartheta\right)^2 (1 - \sin^2\vartheta) = \left(\frac{m U_n^2}{q E_{\text{conv}} r_c}\right)^2 \sin^2\vartheta \qquad (E5)$$

$\sin\vartheta$ is a root of the following 4th-degree polynomial:

$$\sin^4\vartheta - \frac{2\rho}{r_c} \sin^3\vartheta + \left(\frac{\rho^2}{r_c^2} - 1 + \left(\frac{m U_n^2}{q E_{\text{conv}} r_c}\right)^2\right) \sin^2\vartheta$$

$$+ \frac{2\rho}{r_c} \sin\vartheta - \frac{\rho^2}{r_c^2} = 0 \qquad (E6)$$

with explicit expression (cf. Ferrari method) but not straightforward to derive. For $\left(\frac{m U_n^2}{q E_{\text{conv}} r_c}\right)^2 \sim o(1)$ (here $\sim$0.0062; see Table 1), the roots are trivial (i.e. 1 and ρ/r_c) and the limit of the wake is:

$$z(\rho, \vartheta) = \sqrt{r_c^2 - \rho^2} \qquad \text{if } \rho \leq r_c \ (\sin\vartheta = \rho/r_c)$$

$$= -\frac{qE_{\text{conv}}}{2mU_n^2}(\rho - r_c)^2 \text{ if } \rho \geq r_c \ (\sin\vartheta = 1) \qquad (E7)$$

The wake plays a key role and is a boundary. On the one hand, between the comet and the wake, the ion dynamics is dominated by the initial velocity of ions so that the ion distribution is expected to follow the Haser (1957) model. On the other hand, far from the wake, the electric field has enough time to accelerate the ions, which reach velocities significantly higher than their initial one. Then the ion number density from the simplified model (see Fig. G1, middle panel) is expected to follow more likely the original model from Vigren et al. (2015).

APPENDIX F: MATHEMATICAL DEMONSTRATION OF THE APPROACH BY VIGREN ET AL. (2015)

The goal of this Appendix is to rigorously demonstrate the formula proposed by Vigren et al. (2015), here referred as equation (11).

Let's consider four vertices of the volume element in the position space and let's assess how it varies from the position S_0 to S_1 (cf. Fig. 2). The position of the first vertex A with respect to the time is given by:

$$x_A(t) = (r_0 + U_n t)\cos\varphi_0 \sin\theta_0$$

$$y_A(t) = (r_0 + U_n t)\sin\varphi_0 \sin\theta_0$$

$$z_A(t) = (r_0 + U_n t)\cos\theta_0 - \frac{qE}{2m}t^2 \qquad (F1)$$

where r_0 stands for the initial distance, θ_0, for the initial colatitude, and φ_0, for the initial longitude of the ion when it is produced. Let's consider three other vertices (B, C, D) separated from (x_A, y_A, z_A), respectively, by an infinitesimal variation of Δr (B), $\Delta\theta$ (C), and $\Delta\varphi$ (D):

$$x_B(t) = (r_0 + \Delta r + U_n t)\cos\varphi_0 \sin\theta_0$$

$$y_B(t) = (r_0 + \Delta r + U_n t)\sin\varphi_0 \sin\theta_0$$

$$z_B(t) = (r_0 + \Delta r + U_n t)\cos\theta_0 - \frac{qE}{2m}t^2 \qquad (F2)$$

$$x_C(t) = (r_0 + U_n t)\cos\varphi_0 \sin(\theta_0 + \Delta\theta)$$

$$y_C(t) = (r_0 + U_n t)\sin\varphi_0 \sin(\theta_0 + \Delta\theta)$$

$$z_C(t) = (r_0 + U_n t)\cos(\theta_0 + \Delta\theta) - \frac{qE}{2m}t^2 \qquad (F3)$$

$$x_D(t) = (r_0 + U_n t)\cos(\varphi_0 + \Delta\varphi) \sin\theta_0$$

$$y_D(t) = (r_0 + U_n t)\sin(\varphi_0 + \Delta\varphi) \sin\theta_0$$

$$z_D(t) = (r_0 + U_n t)\cos\theta_0 - \frac{qE}{2m}t^2 \qquad (F4)$$

The volume element $V(t)$ in the position space for small Δr, $\Delta\theta$, and $\Delta\varphi$, is given by:

$$V(t) = |\det(\boldsymbol{AB}(t), \boldsymbol{AC}(t), \boldsymbol{AD}(t))| = (r_0 + U_n t)^2 \sin\theta_0 \Delta r \Delta\theta \Delta\varphi \qquad (F5)$$

such as, at t when the ion reaches S_2 (or S_1 in the absence of forces; see Fig. 2):

$$V_2 = V(t) = V(0)(r_0 + U_n t)^2/r_0^2 = r_1^2/r_0^2 \qquad (F6)$$

where r_1 is the distance of S_1 from the comet. This behaviour results from the following reasons:

(i) The force applied to the ion is independent of the position.

(ii) A slight displacement of the ion position induces a slight displacement of the velocity, which is not occurring in the general kinetic picture as the velocity is independent of the position. If the ion was not produced with a single velocity but according to a distribution function, this assertion would not be true any longer.

(iii) The initial velocity is radial ($\nabla \cdot \boldsymbol{U}_n \neq 0$).

Let ΔN_0 be the number of particles produced at S_0 during a short time Δt: $\Delta N_0 = \nu_{\text{ion}} n_n(r_0) V(0)\Delta t = \nu_{\text{ion}} n_n(r_0) r_0^2 \sin\theta_0 \Delta r \Delta\theta \Delta\varphi \Delta t$.[2] Along the trajectory, the number of particles is conserved under conservative forces (Liouville's theorem) such that N_0 is constant up to the position S_2.[3] However, as the volume element has changed, the ion number density changed such that at S_2 it is given by: $\Delta n_{\text{ion}} = \Delta N_0/V_2 = \nu_{\text{ion}} n_n(r_0)(r_0/r_1)^2 \Delta t \nu_{\text{ion}} n_n(r_1 \Delta t)$ which yields:

$$\frac{\mathrm{d}n_{\text{ion}}(\rho, z, t)}{\mathrm{d}t} = \nu_{\text{ion}} n_n(r_1) \qquad (F7)$$

where (ρ, z) is the position of S_2, r_1 is the cometocentric distance of S_1 with the coordinates at the position $(\rho, z + qE_{\text{conv}}t^2/2m)$, depending on time. By integrating over time, one gets equation (11). The same approach can then be applied to derived other moments such as the mean velocity and the velocity dispersions.

APPENDIX G: ANALYTICAL DERIVATION FOR VIGREN ET AL. (2015)

We propose an analytical approximation of the ion number density and mean velocity provided in Vigren et al. (2015) assuming $C_\tau = 1$ everywhere such that (from equations 5 and 11):

$$n_{\text{ion,V}}(x, y, z) = \int_0^{+\infty} \frac{\nu_{\text{ion}} Q}{4\pi U_n} \frac{1}{\rho^2 + \left(z + \frac{qE\tau^2}{2m}\right)^2} \, \mathrm{d}\tau$$

$$n_{\text{ion,V}}(x, y, z) = \frac{\nu_{\text{ion}} Q}{4\pi U_n} \int_0^{+\infty} \frac{1}{\rho^2} \frac{1}{1 + \left(\frac{z}{\rho} + \frac{qE\tau^2}{2m\rho}\right)^2} \, \mathrm{d}\tau \qquad (G1)$$

By introducing $a = \frac{z}{\rho}$, $b^2 = \frac{2m\rho}{qE}$ (the electric field is downward, E is positive, the direction is already taken into account) and $T = \tau/b$, equation (G1) becomes:

$$n_{\text{ion,V}}(x, y, z) = \frac{\nu_{\text{ion}} Q}{4\pi U_n} \int_0^{+\infty} \frac{b}{\rho^2} \frac{1}{1 + (a + T^2)^2} \, \mathrm{d}T$$

We need to determine the four poles of the function which are given by:

$$T = \pm(-a \pm i)^{1/2} = \pm\sqrt[4]{a^2 + 1}\, \exp\left(\pm i\frac{\psi}{2}\right) = \pm\sqrt{\frac{r}{\rho}}\, \exp(\pm i\zeta)$$

[2] We are considering the number of particles and not the distribution function as, in the velocity space, the production term is reduced to $\delta^3(\boldsymbol{v}(t))$.

[3] During the ion motion, the ion angular momentum is strictly decreasing from 0 such that one trajectory does never cross another ion production site except in the absence of force.
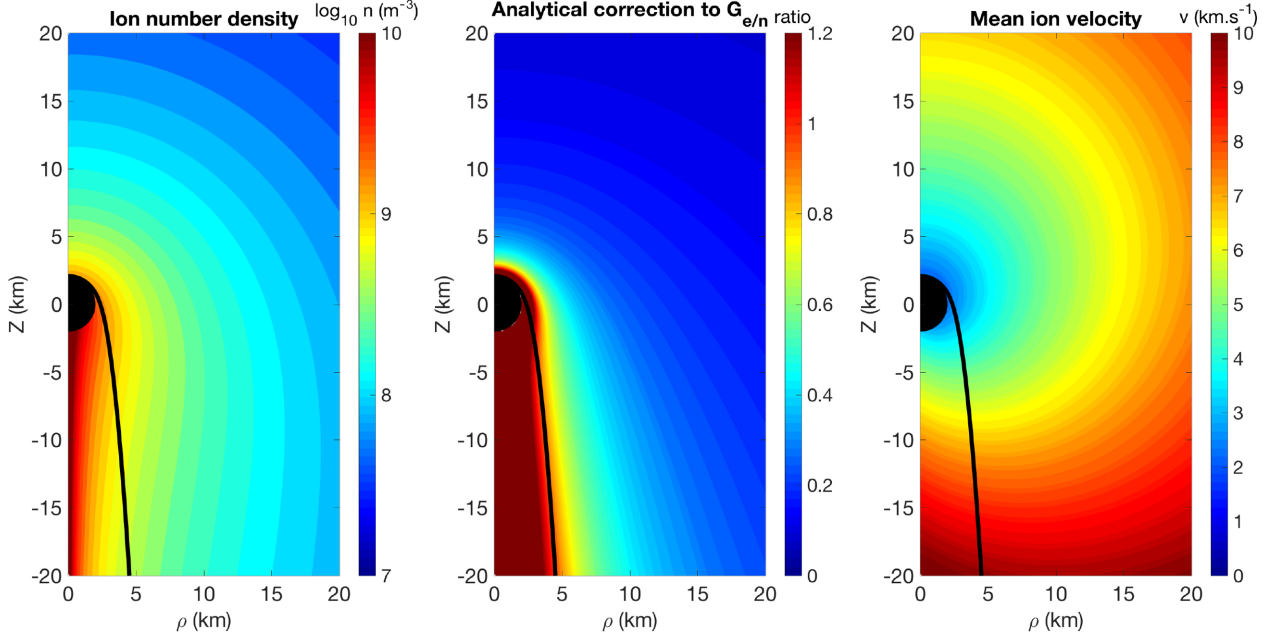
Figure G1. Contours for analytical derivations from Vigren et al. (2015): (left) ion number density $n_{\text{ion, V}}$, (middle) the ion-neutral ratio n_{ion}/n_n with respect to the Haser (1957) model from our analytical formula (i.e. $G_{e/n}$ correction factor of Vigren et al. (2015) $n_{\text{ion, V}}/n_{\text{ion, H}}$), and (right) mean perpendicular velocity. The inputs are the same: $Q = 10^{27}$ s^{-1}, $U_n = 650$ m s^{-1}, $\nu_{\text{ion}} = 6.10^{-8}$ s^{-1}, $E_{\text{conv}} = 5.10^{-4}$ V m^{-1} (see Table 1). These plots are perfectly in agreement with ones from Vigren et al. (2015) and Model B, except within the wake.

where $R = \sqrt{r/\rho}$, $\psi = \arg(-z + i\rho) = \pi - \arccos\left(\frac{z}{r}\right) = \pi - 2\zeta$ such that $\zeta \in \left[0; \frac{\pi}{2}\right]$.

Now, we should perform a partial fraction decomposition:

$$\frac{1}{1 + \left(a + T^2\right)^2} = \frac{A_1}{T - R\exp(i\zeta)} + \frac{A_2}{T - R\exp(-i\zeta)}$$
$$+ \frac{A_3}{T + R\exp(i\zeta)} + \frac{A_4}{T + R\exp(-i\zeta)} \quad \text{(G2)}$$

$$A_1 = \frac{1}{2iR\sin\zeta}\frac{1}{2R\exp(i\zeta)}\frac{1}{2R\cos\zeta} = \frac{1}{8iR^3\sin\zeta} - \frac{1}{8R^3\cos\zeta}$$

$$A_2 = \frac{1}{-2iR\sin\zeta}\frac{1}{2R\cos\zeta}\frac{1}{2R\exp(-i\zeta)}$$

$$A_3 = \frac{1}{-2R\exp(i\zeta)}\frac{1}{-2R\cos\zeta}\frac{1}{-2iR\sin\zeta}$$

$$A_4 = \frac{1}{-2R\cos\zeta}\frac{1}{-2R\exp(-i\zeta)}\frac{1}{2iR\sin\zeta}$$
$$= \frac{1}{8iR^3\sin\zeta} + \frac{1}{8R^3\cos\zeta}$$

As the integrand is holomorphic on $\mathbb{C}$ except at the poles, we can apply the residue theorem on the contour going along the real axis and then counter-clockwise along the semicircle going for $+\infty$ to $-\infty$. One then finds:

$$2\int_0^{+\infty}\frac{1}{1 + \left(a + T^2\right)^2}dT = \int_{-\infty}^{+\infty}\frac{1}{1 + \left(a + T^2\right)^2}dT$$
$$= 2i\pi(A_1 + A_4) \quad \text{(G3)}$$

because $R\exp(i\zeta)$ and $-R\exp(-i\zeta)$ are within this contour. The result is:

$$A_1 + A_4 = \frac{1}{4iR^3\sin\zeta} = \frac{\rho\sqrt{\rho}}{4ir\sqrt{r}\sqrt{\frac{1 - \cos\psi}{2}}}$$

Thus, equation (G3) becomes:

$$\int_0^{+\infty}\frac{1}{1 + \left(a + T^2\right)^2}dT = \frac{1}{2}\int_{-\infty}^{+\infty}\frac{1}{1 + \left(a + T^2\right)^2}dT$$
$$= \frac{\pi\rho\sqrt{2\rho}}{4r\sqrt{r + z}}$$

$$n_{\text{ion, V}}(x, y, z) = \frac{\nu_{\text{ion}}Q}{4\pi U_n\rho^2}\sqrt{\frac{2m\rho}{qE}}\frac{\pi\rho\sqrt{2\rho}}{4r\sqrt{r + z}} = \frac{\nu_{\text{ion}}Q}{8U_n r}\sqrt{\frac{m}{qE(r + z)}}$$

For the mean flux, we have:

$$n_{\text{ion, V}}\langle v_\parallel\rangle_V(x, y, z) = -\frac{\nu_{\text{ion}}Q}{4\pi U_n}\int_0^{+\infty}\frac{\frac{qE\tau}{m}}{\rho^2 + \left(z + \frac{qE\tau^2}{2m}\right)^2}d\tau$$

as proposed by Vigren et al. (2015). Performing the same substitutions as before, one gets:

$$n_{\text{ion, V}}\langle v_\parallel\rangle_V(x, y, z) = -\frac{\nu_{\text{ion}}Q}{4\pi U_n\rho}\int_0^{+\infty}\frac{2T}{1 + \left(a + T^2\right)^2}dT$$
$$= \frac{\nu_{\text{ion}}Q}{4\pi U_n\rho}\left(\frac{\pi}{2} - \arctan(a)\right) \quad \text{(G4)}$$

Through trigonometry, assuming $\rho \neq 0$, we finally obtain:

$$n_{\text{ion,V}} \langle v_{\parallel} \rangle_{\text{V}} (x, y, z) = -\frac{v_{\text{ion}} Q}{4\pi U_n \rho} \arccos\left(\frac{z}{r}\right)$$

One can check that:

$$\frac{\partial (n_{\text{ion,V}} \langle v_{\parallel} \rangle_{\text{V}})}{\partial z} = \frac{v_{\text{ion}} Q}{4\pi U_n r^2}$$

The flux along the z-axis is already fulfilling the continuity equation where the right-hand side corresponds to the production rate, without having to consider the lateral transport.

This paper has been typeset from a TEX/LATEX file prepared by the author.